WILEY-VCH

DOI: 10.1002/adma.(please insert DOI)

Multiple Cations Nanoconfinement in Ultrathin V_2O_5 Nanosheets Enables Ultrafast Ion Diffusion Kinetics toward High-performance Zinc Ion Battery

*Yang Liu, Chengjie Lu, Yunting Yang, Wenshu Chen, Fei Ye, Hongliang Dong, Yuping Wu, Renzhi Ma, Linfeng Hu**

---

[*] Prof. L. F. Hu, W.S. Chen, Y. Liu, Y. T. Yang, C. J. Lu, F. Ye

School of Materials Science and Engineering, Southeast University

Nanjing, 211189, P. R. China

These authors contributed equally: Y. Liu, Dr. C. J. Lu

*Email: linfenghu@seu.edu.cn

Dr. H. L. Dong

Center for High Pressure Science and Technology Advanced Research, Shanghai, 201203, P. R. China

Prof. Y. P. Wu

School of Energy and Environment, Southeast University, Nanjing 211189, P. R. China

Prof. R. Z. Ma

Research Center for Materials Nanoarchitectonics, National Institute for Materials Science (NIMS), Namiki 1-1, Tsukuba, Ibaraki 305-0044, Japan.

Abstract

Aqueous zinc-ion battery shows great potential and considerable interest in the energy storage field, and the nanoconfinement of cations in layered oxide cathode is an important approach to realize advanced zinc ion storage on capacity and cycling stability. However, thus far, the conventional hydrothermal/solvothermal route for this nanoconfinement has been restricted to its uncontrollable phase structure and the difficulty on the multiple cation co-confinement simultaneously. Herein, we reported a general, supramolecular self-assembly of ultrathin V_2O_5 nanosheets using various unitary cations including Na^+, K^+, Mg^{2+}, Ca^{2+}, Zn^{2+}, Al^{3+}, NH_4^+ and multiple cations ($NH_4^+ + Na^+$, $NH_4^+ + Na^+ + Ca^{2+}$, $NH_4^+ + Na^+ + Ca^{2+} + Mg^{2+}$). The unitary cation confinement results in a remarkable increase in the specific capacity and Zn-ion diffusion kinetics, and the multiple cation confinement gives rise to superior structural and cycling stability by multiple cation synergetic pillaring effect. The optimized diffusion coefficient of Zn-ion (7.5×10^{-8} cm^2 s^{-1}) in this assembly series surpasses most of the V-based cathodes reported up to date. Density functional theoretical (DFT) simulation further reveals a declined Zn-ion diffusion barrier by cation confinement due to a significantly weakened interaction between Zn^{2+} and the dangling oxygen atom of V_2O_5. Our work develops a novel multiple-cations nanoconfinement strategy toward high-performance cathode for aqueous battery. It also provides new insights into the guest cation regulation of zinc-ion diffusion kinetics through a general, supramolecular assembly pathway.

Keywords:

supramolecular assembly; nanoconfinement; multiple cations; ion diffusion kinetic; aqueous zinc-ion battery

1. Introduction

The rapid development of gird-scale energy storage and flexible electronics has triggered tremendous demands in advanced rechargeable battery systems beyond lithium-ion batteries [1,2]. Among them, aqueous zinc-ion batteries (AZIBs) are gaining considerable attention [3-5]. As the next generation of large-scale energy storage units due to their advantages in high theoretical capacity (820 $mAh \cdot g^{-1}$ and 5854 $mAh \cdot cm^{-3}$; low redox potential (-0.763 V versus standard hydrogen electrode); high safety and low cost. [6-8] During the past few years, great progress has been made to demonstrate a lot of novel AZIBs cathode materials including inorganic Mn, V, Mo-based oxides/sulfides, and metal-organic compounds of Prussian blue analogous (PBAs) [9-15]. Among them, manganese-based materials suffer from Mn^{2+} dissolution caused by the Jahn-Teller effect and also the fast fade of capacities [16-18]. Prussian blue analogues always deliver inferior specific capacity (< 60 $mAh \cdot g^{-1}$) and low voltage plateau (0.7 V vs. Zn/Zn^{2+}) [19-21]. Vanadium-based compounds are very promising and received extensive attention owing to their remarkable advantage on specific capacity [3,22-24].

Especially, recent progress revealed that a cation nanoconfinement strategy in vanadium oxides can significantly improve its electrochemical properties due to the as-embedded metallic cations acting as pillars in the layered frameworks and expanding the interlayer spacing to facile Zn ion diffusion. For example, Zhou et al synthesized $Li_xV_2O_5 \cdot nH_2O$ nanosheets cathode by a hydrothermal treatment of V_2O_5 and $LiNO_3$ solution with the assistance of H_2O_2[25]. Alshareef disclosed that $Ca_{0.24}V_2O_5 \cdot 0.83H_2O$ nanobelts, prepared through a hydrothermal process of $CaCl_2$ and V_2O_5 mixed solution[26]. Although the hydrothermal/solvothermal route can synthesize a series of $M_xV_2O_5 \cdot nH_2O$ (M = Li, Ca, Zn, Na, Mn, Co, Cu, Zn, Al, Cr, Ag, etc.) [27], these $M_xV_2O_5 \cdot nH_2O$ derivates generally cannot be crystallized in the same phase structure. Furthermore, it is also impossible to embed multiple cations simultaneously in the host through the hydrothermal/solvothermal route, making the difficulty on material design, property

optimization, and understanding on host-guest interlayer chemistry. Accordingly, developing a general strategy for cation nanoconfinement strategy is essential but still very challenging.

Layered materials have been well recognized in electrochemical energy storage owing to its rich intercalation chemistry and very high active surface [28-31]. More importantly, two-dimensional (2D) nanosheets with single-layer to multiple-layer thickness obtained from their layered bulk precursor can be regarded as inorganic supermolecules [32]. As soon as adding some oppositely charged ions or molecules into this 2D nanosheet colloidal system, re-stacking of the nanosheets driven by electrostatic interaction occurs immediately to form some flocculent precipitate, which can be easily recovered by filtration or low-speed centrifugation [30-32].

Inspired by this phenomenon, we consider it is possible to realize a general strategy for cation nanoconfinement in the layered V_2O_5 host for superior zinc ion storage. Herein, we reported a general supramolecular self-assembly of ultrathin V_2O_5 nanosheets induced by various metallic and non-metallic cations (**Scheme 1**). A series of $M_xV_2O_5{\cdot}nH_2O$ ($M = NH_4^+$, Li^+, Na^+, K^+, Mg^{2+}, Ca^{2+}, Zn^{2+}, Al^{3+}) can be easily synthesized by this strategy. More interestingly, we can realize a simultaneously cooperative confinement of several cations (NH_4^+/Na^+, $NH_4^+/Na^+/Ca^{2+}$, $NH_4^+/Na^+/Ca^{2+}/Mg^{2+}$) by this strategy. We make a systematic comparison on the Zn^{2+} storage capacity, long-term cycling stability and Zn^{2+} diffusion kinetics on this self-assemble series. The unitary cation confinement results in superior storage capacity and very fast Zn-ion diffusion kinetics. The optimized diffusion coefficient of zinc ion (7.5×10^{-8} cm^2 s^-) in this assembly series surpasses most of the V-based cathodes reported up to date. DFT simulation further reveals a declined Zn-ion diffusion barrier by unitary cation nanoconfinement due to a significantly weakened interaction between Zn^{2+} and dangling oxygen atom of V_2O_5. The multiple cation confinement gives rise to an enhancement on the long-term cyclability and structural stability by multiple cation synergetic pillaring effect.

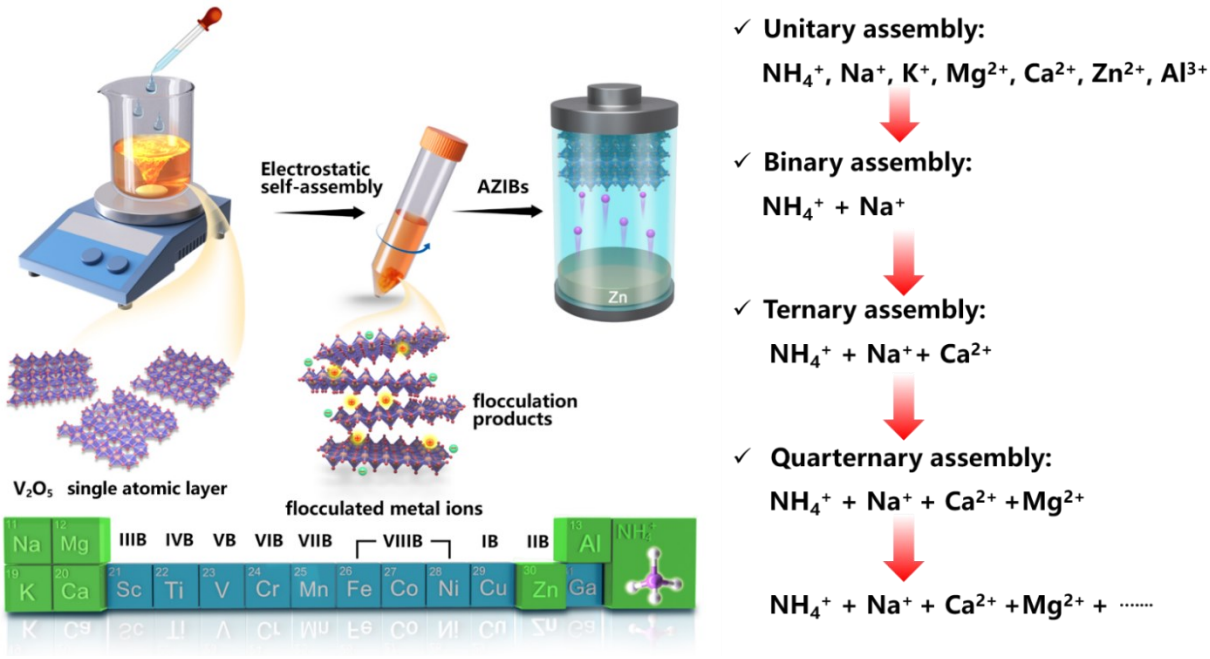

Scheme 1. Schematic illustration for the supramolecular self-assembly strategy.

2. Results and Discussion

Supramolecular assembly of NH_4^+. V_2O_5 colloid suspension was prepared by a simple hydrothermal method reported previously [33]. One liter of aqueous colloid with a clear Tyndall light scattering can be produced (Figure 1a, b). Transmission electron microscopy (TEM) observation further reveals numerous thin sheet-like objects with a lateral size of 200 –300 nm and wrinkled edges (Figure 1c-d). The corresponding selected area electron diffraction (SAED) pattern (Figure 1d) presents typical polycrystalline rings due to the overlap of these nanosheets. Atomic force microscopy (AFM) characterization also detects two-dimensional ultrathin sheets with a lateral dimension in the range of 300–400 nm (Figure 1e). The height profile in Figure 1f demonstrates a thickness of 0.40–0.53 nm, which is very close to the crystallographic thickness (0.44 nm) of V_2O_5 single atomic layer (Figure 1g). Known that most of the unilamellar oxide nanosheets can be regarded as a kind of Bronsted acid group, which can adsorb positive charged species [34]. Herein, the average zeta potential of the resulting V_2O_5 colloid suspension

is determined as −60.4 mV, suggesting the possibility of colloidal self-assembly by some positively charged ions.

Then we first selected NH_4^+ as the anti-cation to verify the self-assembly behavior. Flocculation phenomenon immediately occurred by mixing the colloidal suspension with 0.2 M NH_4Cl aqueous solution to form apparent needle-like precipitation at the bottom of the colloidal suspension, and the orange colloid gradually transformed into colorless transparent. After the flocculation, the product was aged for several hours in this solution with continuous magnetic stirring to tune its zinc ion storage capacity as discussed below. X-ray diffraction (XRD) patterns of the flocculation product after aging are given in Figure S1a (Supporting Information). The sharp peaks around 5~9° can be indexed as (001) basal series, of which the d-spacing can be regarded as the basal spacing of the re-stacked structure. Note that some out-plane (*hkl*, $l \neq 0$) diffraction peaks can also be detected in both freeze-dried V_2O_5 powder and the NH_4^+ flocculation product, demonstrating that the yield of the single-layer V_2O_5 nanosheets cannot reach up to 100 % with the presence of some multilayered structure in the as-prepared V_2O_5 nanosheets [30, 35]. Compared to the freeze-dried sample obtained from the V_2O_5 colloid suspension, the 00*l* (*l* =1, 2, 3, 4, 5, 6) characteristic peaks exhibit a shift towards larger diffraction angle for our NH_4^+ flocculation product, indicating the slight decrease in the basal spacing from 11.6 to 11.1 Å due to the host-guest interaction between NH_4^+ and the V_2O_5 single layer [36]. The thermogravimetric (TG) analysis of the as-prepared sample measured in the temperature range of 25 – 600 °C was carried out (Figure S1b, Supporting Information). The weight loss below 50 °C (domain I) is ascribed to the removal of absorbed water, and the loss between 50 and 145 °C (domain II) should be assigned to the evaporation of the crystal water. Moreover, the loss after 145℃ (domain III) could be ascribed to the evaporation of the intercalated NH_4^+ cations[37, 38], which was further confirmed by the XRD pattern of the NH_4^+ flocculation sample after 400℃ (Figure S1c, Supporting Information). Thus, the chemical formula of as-prepared flocculation product can be identified as $(NH_4)_{0.77}V_2O_5 \cdot 0.8H_2O$.

Scanning electron microscopy (SEM) observation of the self-assembled sample reveals large-sized agglomerations with lateral size up to several micrometers due to the stacking of V_2O_5 nanosheets (Figure 1h). Transmission electron microscope (TEM) images (Figure 1i-j) show two-dimensional nanoribbon morphology, suggesting the nanosheets might be drastically fractured into nanoribbons during the restacking. High-resolution transmission electron microscopy (HRTEM) images taken from the nanoribbon surface in Figure 1k exhibited a clear two-dimensional lattice fringe, and the 0.202, 0.195 nm spacing of which agrees well with the expected separation of (006), (120) planes of layered V_2O_5, respectively. Energy dispersive spectrum (EDS) mapping (Figure 1l) reflects the uniform distribution of V and O elements in the sample, and the appearance of N element distribution confirms the successful NH_4^+ embedding in the layered $V_2O_5{\cdot}nH_2O$ host.

Subsequently, the zinc-ion battery performance was investigated in CR-2032 coin cells using a Zn foil anode, 2.0 M $Zn(OTf)_2$ electrolyte, and a glass fiber separator. Interestingly, we found the specific capacity is highly dependent on the aging time after the self-assembly process. As shown in Figure 1m, the $(NH_4)_{0.77}V_2O_5{\cdot}0.8H_2O$ sample aged at 1 h, 1.5 h, 2 h, 2.5 h, 4 h, and 5 h exhibits a discharge capacity of 246.3, 317.8, 340.7, 359.2, 388.8, and 394.5 mA h g^{-1} at 100 mA g^{-1}, respectively (Figure 1m). Further increase in the aging time leads to the saturated capacity at this threshold time. Ultimately, the specific capacity (C) versus aging time (t) can be fitted as an exponential growth tendency as follows:

$$\boldsymbol{C = -250e^{-0.55t} + 417}$$

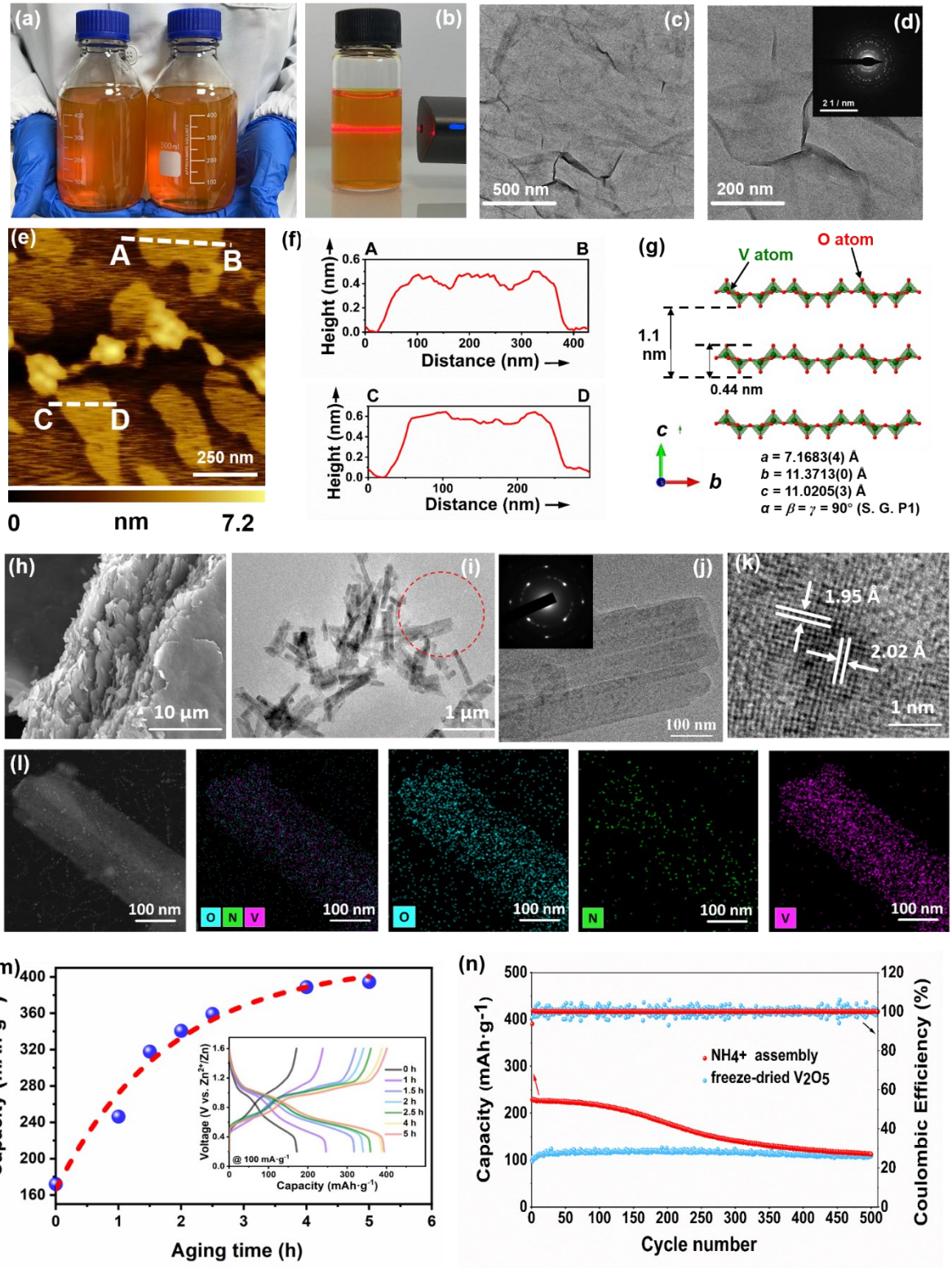

Figure 1. (a) Liter-scale preparation of the V_2O_5 nanosheet colloidal. **(b)** Tyndall effect of V_2O_5 colloidal. **(c, d)** TEM images of the V_2O_5 nanosheets and the corresponding SAED pattern. **(e)** AFM images and **(f)** the corresponding height profiles. **(g)** Schematic illustration of the layered V_2O_5 crystal structure and its single atomic layer height. **(h)** SEM image, **(i, j)** TEM image and SAED pattern, **(k)** HRTEM image, **(l)** EDS mapping images of $(NH_4)_{0.77}V_2O_5 \cdot 0.8H_2O$ sample.

(**m**) An exponential growth on specific capacity with the aging time of the as-prepared $(NH_4)_{0.77}V_2O_5{\cdot}0.8H_2O$ cathode at a current density of 0.05 $A{\cdot}g^{-1}$. Inset is the corresponding GCD profiles at various aging time. (**n**) Long-term cycling stability at 5.0 $A{\cdot}g^{-1}$.

The phase evolution of this self-assembled sample during the aging process was identified by XRD patterns (Figure S2, Supporting Information). For the fresh flocculation sample without any aging treatment, the presence of asymmetric diffraction peaks at 47.2°, 50.8°, and 60.5° with a tail toward a higher angular side is a typical characteristic of a disordered lamellar structure. According to the previous study[30], the V_2O_5 single-layer nanosheets were restacked with well maintain of the in-plane atomic arrangement but losing its regular sheet-stacking sequence. However, these asymmetric diffraction peaks converted into symmetrical after 1 h – 5 h aging, indicating such a disordered lamellar structure may recrystallize into a three-dimensional ordered crystal. Careful SEM observation indicates that the surface of the sample aging at 1 h exhibits restacked sheet morphology with a very smooth surface (Figure S3, Supporting Information). With prolonging the aging time, the surface generally converted to rather rough and porous, which should be responsible for the as-observed capacity increase in Figure 1m. CV curves with varied scan rates give a vital dependence of the peak current density and scan rate to clarify the capacity contribution type for Zn-ion storage (Figure S4, Supporting Information).[39-40] The capacitive contribution can be calculated as 59.3%, 67.6%, 75.0%, 81.0%, 86.3%, and 91.0% at the scan rate of 0.1, 0.2, 0.4, 0.6, 0.8, and 1.0 mV s^{-1}, respectively. *Ex situ* XRD characterization identifies a typical Zn^{2+} intercalation/de-intercalation mechanism of our $(NH_4)_{0.77}V_2O_5{\cdot}0.8H_2O$ sample the same as the most V-based cathodes reported previously (Figure S5, Supporting Information). Figure S6 (Supporting Information) gives the rate performance of $(NH_4)_{0.77}V_2O_5{\cdot}0.8H_2O$ electrode with the average capacities of 366.2, 290.6, 244.1, 204.2,177.5 and 165.4 mAh g^{-1} at the current densities of 0.05, 0.1, 0.2, 0.5, 0.8, 1.0 A g^{-1}, respectively. When the current density was reset to 0.05 A g^{-1}, a recovered capacity of 363.2 mA h g^{-1} was achieved. The long-term cyclability of our as-assembled

$(NH_4)_{0.77}V_2O_5{\cdot}0.8H_2O$ sample is depicted in Figure 1n. Although the cycle stability decreases after NH_4^+ nano-confining, its initial capacity is remarkably higher than that of the bare V_2O_5 freeze-dried sample.

Extend to other guest cations. We found our supramolecular colloidal self-assembly strategy can be easily extended to other guest cations such as Li^+, Na^+, K^+, Mg^{2+}, Ca^{2+}, Zn^{2+}, Al^{3+}. Needle-like precipitation can be clearly observed expect the case of Li^+ which exhibits very fine sediment hardly been recovered by filtration or high-speed centrifugation (Figure 2a). In the case of Li^+ assembly, any sediment cannot be observed and the TEM image (Figure S7, Supporting Information) shows no apparent morphology differences compared with the original nanosheet. We consider that the Li^+ might not make the re-stacking of V_2O_5 nanosheets through electrostatic force due to the relatively smaller surface charged density of Li^+ compared with other cations (Mg^{2+}, Ca^{2+}, Zn^{2+}, Al^{3+}). SEM observation (Figure S8, Supporting Information) revealed that all samples consisted of large agglomerations due to the stacking of V_2O_5 nanosheets. The chemical formula of these samples flocculated by Na^+, K^+, Mg^{2+}, Ca^{2+}, Zn^{2+}, Al^{3+} were determined by ICP (Supplementary Tab S1) and TGA analysis (Figure S9, Supporting Information), which can be identified as $Na_{0.34}V_2O_5{\cdot}0.46H_2O$, $K_{0.30}V_2O_5{\cdot}0.16H_2O$, $Mg_{0.16}V_2O_5{\cdot}0.82H_2O$, $Ca_{0.14}V_2O_5{\cdot}0.72H_2O$, $Zn_{0.29}V_2O_5{\cdot}0.83H_2O$ and $Al_{0.19}V_2O_5{\cdot}1.19H_2O$, respectively. The comparison of the corresponding XRD patterns (Figure S10, Supporting Information) illustrates its d-spacing of $Al_{0.19}V_2O_5{\cdot}1.19H_2O$ (14.1 Å) > $Ca_{0.14}V_2O_5{\cdot}0.72H_2O$ (13.4 Å) > $Mg_{0.16}V_2O_5{\cdot}0.82H_2O$ (13.3 Å) > $Zn_{0.29}V_2O_5{\cdot}0.83H_2O$ (13.0 Å) > $Na_{0.34}V_2O_5{\cdot}0.46H_2O$, $K_{0.30}V_2O_5{\cdot}0.16H_2O$ (11.2 Å) > $(NH_4)_{0.77}V_2O_5{\cdot}0.8H_2O$ (11.1 Å). Considering the ionic radii order of these metallic ions is: r (Al^{3+}, 50 pm) < r(Mg^{2+}, 65 pm) < r(Zn^{2+}, 74 pm) < r(Na^+, 95 pm) < r(Ca^{2+}, 99 pm) < r(K^+, 133 pm) < r(NH_4^+,143 pm) [41-45], it is unexpected that smaller ion radius result in a larger interlayer spacing in the $M_xV_2O_5{\cdot}nH_2O$ series in principle. Based on the TGA analysis, we hypothesize this phenomenon might be attributed to the discrepancy on hydrated state of different guest cations. This hypothesis was

confirmed by the FTIR and Raman spectra (Figure S11-12, Supporting Information). One can see the Mg^{2+}, Ca^{2+}, Zn^{2+}, Al^{3+}-based samples delivers a much stronger peak at 1614 cm^{-1} assigned to bending vibration peak of the interlayer water than that of bare V_2O_5 nanosheets prepared by freeze drying. In contrast, such a bending vibration enhancement on Na^+, K^+, NH_4^+-based $M_xV_2O_5$ is not very apparent. This result suggests that the as-confined Mg^{2+}, Ca^{2+}, Zn^{2+}, Al^{3+} in V_2O_5 interlayer by our supramolecular self-assembly is highly hydrated. Meanwhile, the other one (Na^+, K^+, NH_4^+) is confined as a low hydration state, leading to a relatively smaller d-spacing.

The zinc-ion storage behavior of this $M_xV_2O_5{\cdot}nH_2O$ (M = Na^+, K^+, Mg^{2+}, Ca^{2+}, Zn^{2+}, Al^{3+}) series was first studied using cyclic voltammetry (CV) at 0.1 mV s^{-1}. As shown in Figure 2b-e, all samples exhibit a very analogous shape with a pair of redox peaks located at 0.9–1.2 V and 0.4–0.8 V, respectively. GCD profiles at 100 mA g^{-1} were well consistent with the CV curves (Figure 2f-i). Figure 2j summarizes the specific zinc ion storage capacities of all $M_xV_2O_5{\cdot}nH_2O$ cathodes in the first cycle, showing a trend with NH_4^+-based $M_xV_2O_5{\cdot}nH_2O$ (394.5 mAh g^{-1}) > Na^+ (281.0 mAh g^{-1}) > K^+ (263.1 mAh g^{-1}) > Mg^{2+}(221.6 mAh g^{-1}) > Ca^{2+} (219.8 mAh g^{-1}) > Zn^{2+} (226.1 mAh g^{-1}) >Al^{3+}(258.6 mAh g^{-1}). It is worth noting that the bare V_2O_5 nanosheet sample just delivers a much smaller capacity of 180 mAh g^{-1}, demonstrating the significant enhancement of zinc ion storage capacity through our supramolecular assembly. XPS spectra identify a reversible $V^{5+}\leftrightarrow V^{4+}/V^{3+}$ transformation during Zn^{2+} insertion and extraction in this $M_xV_2O_5{\cdot}nH_2O$ series (Figure S13, Supporting Information). Electrochemical impedance spectroscopy (EIS) was then performed to investigate the electrochemical kinetics. The corresponding results are collected in Figure 2k, which delivers a semicircle in the high-frequency region and a line in the low-frequency region. After fitting, Mg^{2+}-based $M_xV_2O_5{\cdot}nH_2O$ cathode exhibited the smallest charge transfer resistance (R_{ct}) of 38.85 Ω while Al^{3+}-based $M_xV_2O_5{\cdot}nH_2O$ delivered the highest R_{ct} of 642 Ω (Figure 2k). We further verify the regulation of electronic conductivity using density of states (DOS) by density functional

theoretical（DFT) calculations with a case study of K^+ nanoconfinement. Apparent states of electron density can be found at the Fermi level after cation nanoconfinement, which can be mainly attributed to the shift of Fermi surface towards a high-energy level (Figure S14, Supporting Information). As a result, the electronic conductivity of the nanoconfinement sample is deduced to be better than that of pristine V_2O_5, which is well consistent with the as-achieved R_{ct} results. The rate-capability and long-term cycle performance of Na^+, K^+, Mg^{2+}, Ca^{2+}, Zn^{2+}, Al^{3+} nanoconfinement sample is given in Figure S15-16 (Supporting Information). All of these assembled series deliver superior rate-performance and cycling capacity to that of the bare V_2O_5 freeze-dried sample.

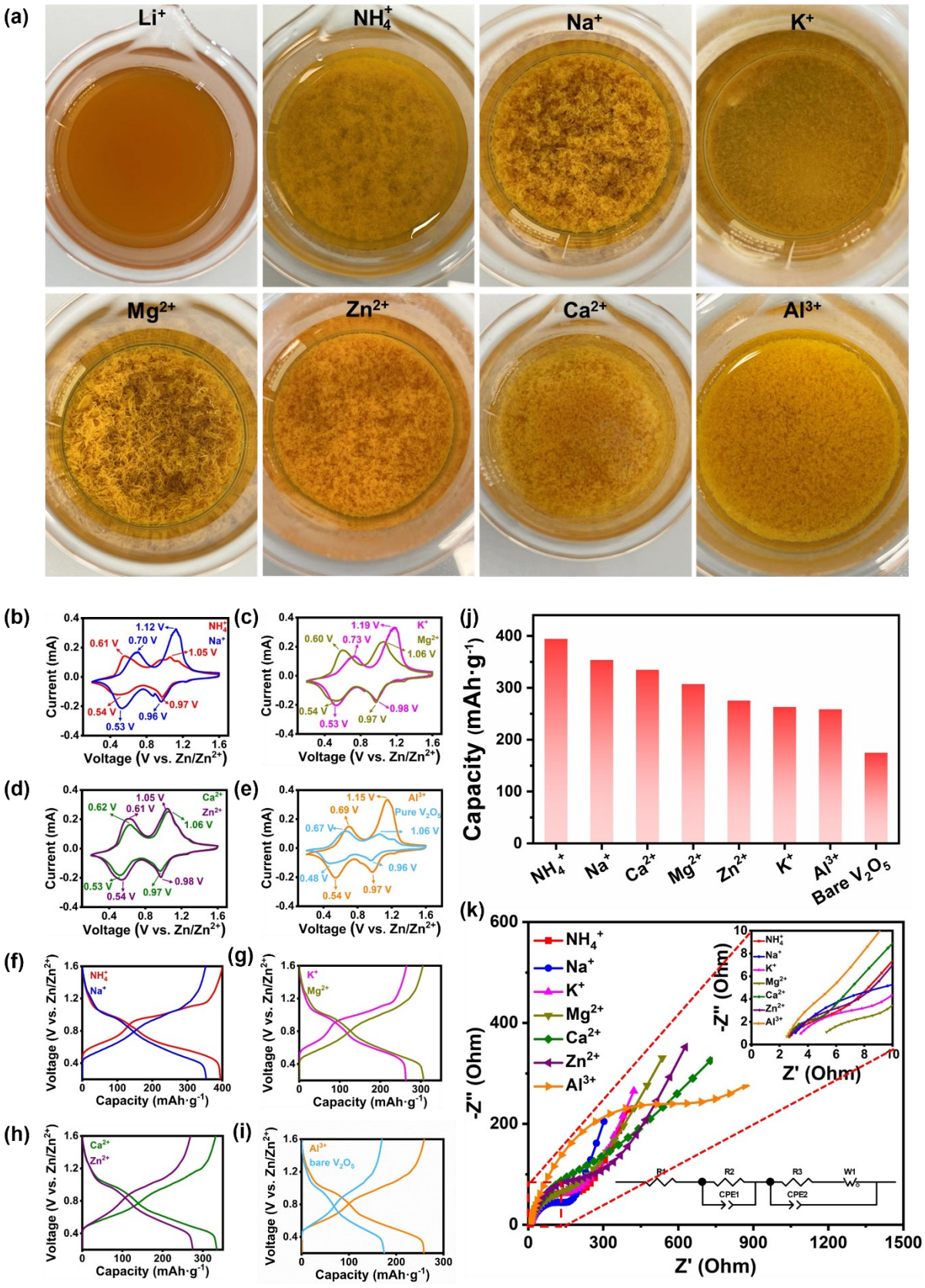

Figure 2. (a) Optical images of the Li^+, NH_4^+, Na^+, K^+, Mg^{2+}, Ca^{2+}, Zn^{2+}, Al^{3+}-based $M_xV_2O_5{\cdot}nH_2O$ flocculation products. **(b-e)** CV profiles and **(f-i)** the corresponding GCD profiles of Na^+, K^+, Mg^{2+}, Ca^{2+}, Zn^{2+}, Al^{3+}-based $M_xV_2O_5{\cdot}nH_2O$ and bare V_2O_5 sample at 0.05

A g^{-1}, respectively. **(j)** Comparison of the discharge specific capacity of $M_xV_2O_5{\cdot}nH_2O$ in the first charge-discharge cycle at 0.05 A g^{-1}. **(k)** EIS spectrum of $M_xV_2O_5{\cdot}nH_2O$ with the enlarged image in high frequency region inserted, showing a degressive trend of R_{ct} with Al^{3+}(642 Ω) > Ca^{2+}(200 Ω) > Na^+(135.4 Ω) > NH_4^+(134 Ω) > Zn^{2+}(120.1 Ω) > K^+(111.6 Ω) > Mg^{2+}(38.85 Ω)

Multiple guest cations cooperative assembly. Interestingly, we found it possible to realize multiple cations confinement in this V_2O_5 host using our self-assembly strategy. When two, three even four kinds of cations sources were simultaneously introduced in the V_2O_5 nanosheet colloid, similar flocculation phenomenon was observed. The corresponding XRD patterns in Figure 3a deliver no significant discrepancy between these unitary, binary, ternary, and quaternary self-assembled series except a shift in the (001) peaks, suggesting the successful confinement of multiple cations. The basal spacing gradually increased from an initial 11.1 Å (NH_4^+) up to 11.4 Å (Na^+ + NH_4^+), 13.6 Å (Na^+ + NH_4^++Ca^{2+}), and then showed a slight decrease to 13.4 Å for quaternary Na^+ + NH_4^+ + Ca^{2+}+ Mg^{2+} confinement. The detailed chemical molar ratio of the various metal cations in the product by ICP atomic emission spectroscopy is listed in Table S2 (Supporting Information). TEM observation and EDS mapping also confirm the success of this multiple guest cations cooperative self-assembly (Figure 3b-d). All of the samples show a lamellar stacking morphology, and the corresponding EDS mapping verifies the uniform distribution of Na, N, Ca, Mg elements in the samples. Strikingly, our self-assembly process shows the advantage compared with the conventional hydrothermal method, which hardly realizes the simultaneous embedding of several cations. When four cations of NH_4^+, Na^+, Mg^{2+}, Ca^{2+} were introduced into the hydrothermal system, the corresponding XRD pattern confirms the product is a mixture of $VO_2{\cdot}nH_2O$ and $CaV_8O_{20}{\cdot}nH_2O$ (Figure S17, Supporting Information).

The success of simultaneous co-assembly of multiple cations in V_2O_5 host endows the opportunity to compare the interlayer cation-dependent performance accurately and to deeply understand the host-guest interlayer chemistry. GCD profiles in Figure S18a (Supporting

Information) show the specific capacity of our self-assembly series and bare V_2O_5 nanosheets. All of the self-assembled samples in this series exhibits a high capacity outperforming that of the bare V_2O_5 nanosheets. On the other hand, with the introduction of more intercalated cations, the capacity gradually decreases from initial 394.5 $mAh \cdot g^{-1}$ to 284.6 $mAh \cdot g^{-1}$. Such a result can be understood by the degressive tendency on specific capacity after unitary NH_4^+, Na^+, Ca^{2+}, and Mg^{2+} confinement (Figure S18b, Supporting Information).

In situ Raman characterization was then employed to investigate the energy storage mechanism of the as-assembled quaternary sample ($Na^+ + NH_4^+ + Ca^{2+} + Mg^{2+}$) as cathodes, which was depicted in a two-dimensional contour image accompanied by the corresponding GCD profile in Figure 3e. Notably, the peak at 150 cm^{-1} attributed to the V-O-V bond slightly shifts to a higher wavenumber and then back to the normal position during discharge/charge processes (see black arrow), indicating that the V-O-V bond was first strengthened by Zn^{2+} adsorption/insertion, then weakened by Zn^{2+} extraction during the charge process. Overall, within the Zn^{2+} insertion in the discharge process, the Raman peaks gradually decreased, demonstrating that the adsorption and insertion of Zn ions break the bonds between V and O atoms inside the cathode crystals. With the potential increasing to 1.6 V, those Raman signals were recovered due to the extraction of Zn ions, demonstrating the good reversibility of our quaternary self-assembled V_2O_5 materials for aqueous Zn ion storage.

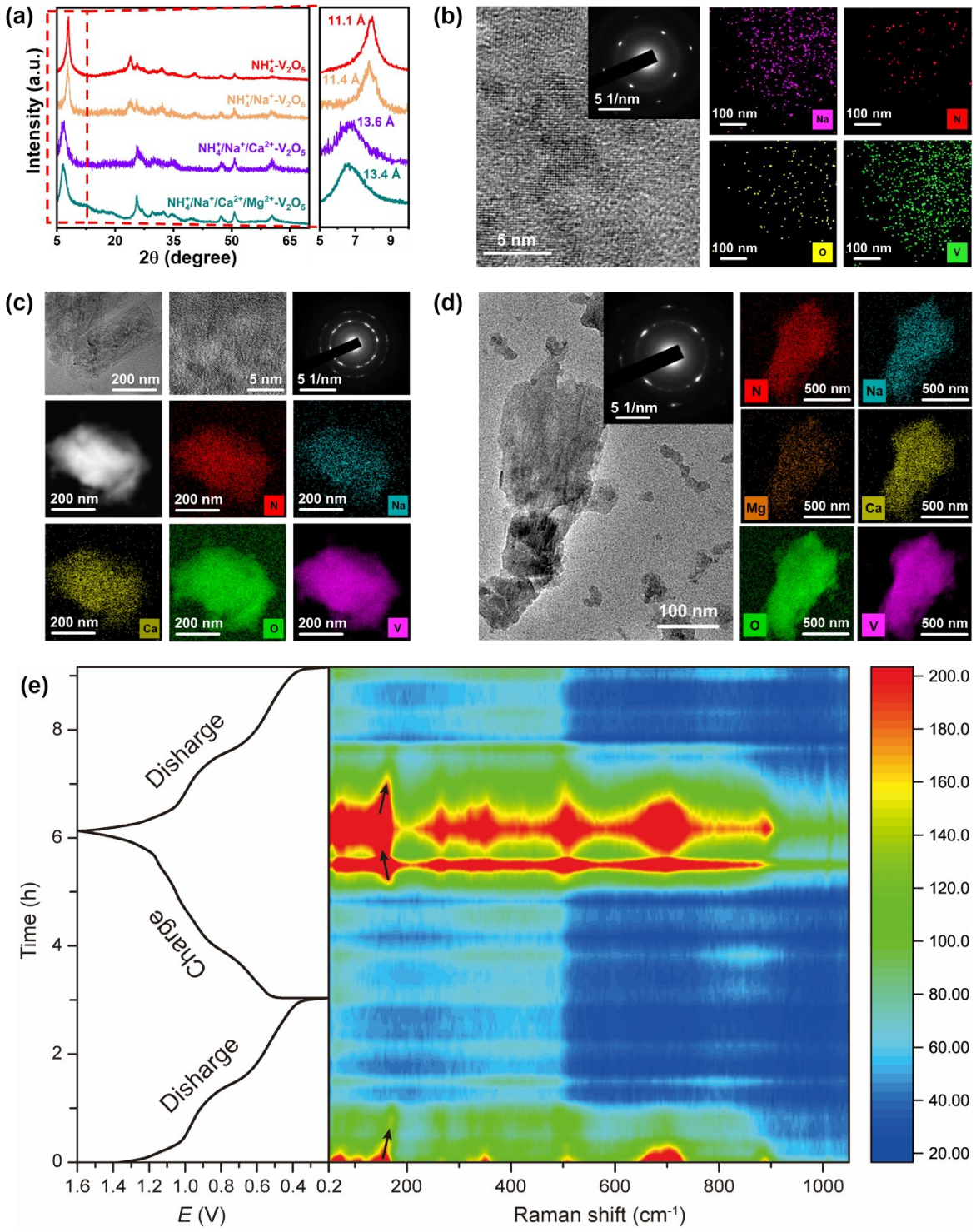

Figure 3. (a) XRD patterns of the NH_4^+, $NH_4^+ + Na^+$, $NH_4^+ + Na^+ + Ca^{2+}$, $NH_4^+ + Na^+ + Ca^{2+} + Mg^{2+}$ cooperative self-assembly products, respectively. HRTEM image and EDS mapping images of **(b)** $NH_4^+ + Na^+$, **(c)** $NH_4^+ + Na^+ + Ca^{2+}$, **(d)** $NH_4^+ + Na^+ + Ca^{2+} + Mg^{2+}$ system. **(e)** *In situ* Raman contour image of our quarternary $NH_4^+ + Na^+ + Ca^{2+} + Mg^{2+}$ assembled sample during the first discharge/charge/discharge processes (at 0.05 A g^{-1}).

Impressively, we found the multiple cations confinement in this V_2O_5 host gives rise to the enhancement on the cycling stability (Figure 4a). With the increase in the category of intercalated guest cations, the multiple cations confinement sample shows a superior long-term stability with a higher capacity retention. The corresponding capacity retention after 1,000 cycles of the $NH_4^+ + Na^+$, $NH_4^+ + Na^+ + Ca^{2+}$ and $NH_4^+ + Na^+ + Ca^{2+} + Mg^{2+}$ cooperative self-assembly products is 37.9%, 80.2%, 88.4%, respectively. Previous work by other groups has revealed that introducing guest species (e.g., metal ions, water molecules, organic molecules, and organometallic molecules) into vanadium-based materials is favorable to relieving the structural deterioration derived from the pillar effect, stabilizing the host structure upon cycling and enlarge the crystal tunnel for more cation occupation[46]. In our case, the improvement in cyclability by multiple cations confinement should be attributed to the increase in the d-spacing and structural stability by multiple cation synergetic pillaring effect [41-45].

DFT calculations were carried out to give a deep understanding on the multiple cation synergetic pillaring effect. Figure 4b shows the atomic configuration of the layered V_2O_5 host with an interlayer distance of 11.6 Å set according to the corresponding XRD characterization in Figure S1. Two types of oxygen atoms can be observed in this V_2O_5 structure respectively: the dangling oxygen (O^D) labeled in green and the bonding oxygen (O^B) labeled in blue. Accordingly, there are two void spaces showing different storage capacities while holding ions or molecules: one is a small void (SV space) surrounded by O^D atoms with a radius around 1.5 Å, and another is a large void (LV space) beneath O^B atoms with a radius above 4.0 Å. It is interesting to find that the O^D atoms shift slightly towards the as-intercalated Na^+ and K^+ due to the large ionic radius of Na^+, K^+, and the long-range affinity effect (depicted in Figure 4b). Figure 4c compares the energy discrepancy while forming M-O^B and M-O^D bonds (M = Na^+, K^+, Mg^{2+}, Ca^{2+}, Zn^{2+}, Al^{3+}). It can be seen that Al^{3+} and Zn^{2+} are energetically favorable for intercalation in the small empty space surrounded by O^D (achieving their maximum formation energy $\Delta E_{MO_4^D}$ of -5.98 eV and -1.72 eV, respectively), while the others including Na^+, K^+, Ca^{2+}

are much more favorable to stay in the large empty space forming M-O^B bonds (achieving their maximum formation energy $\Delta E_{MO_4^B}$ of -3.53 eV, -3.71 eV and -4.86 eV, respectively). By counting the bond length of M-O^B/M-O^D in the optimized $M_xV_2O_5$ structure, the intercalation site of the confined cation is highly dependent on its ionic radius or hydrated ionic radius (Figure 4d). More importantly, the intercalation results given in Figure 4e demonstrated that the energetically preferred accommodation site on the V_2O_5 host for various cations is quite different, accordingly, the increase of intercalated cation species from binary to quaternary guest cations, or even more, can provide a multiple cation synergetic pillaring effect with various cations at different accommodation sites. These multiple guest cations located at different accommodation sites are favorable for a much more stable structure during the zinc-ion insertion and extraction process.

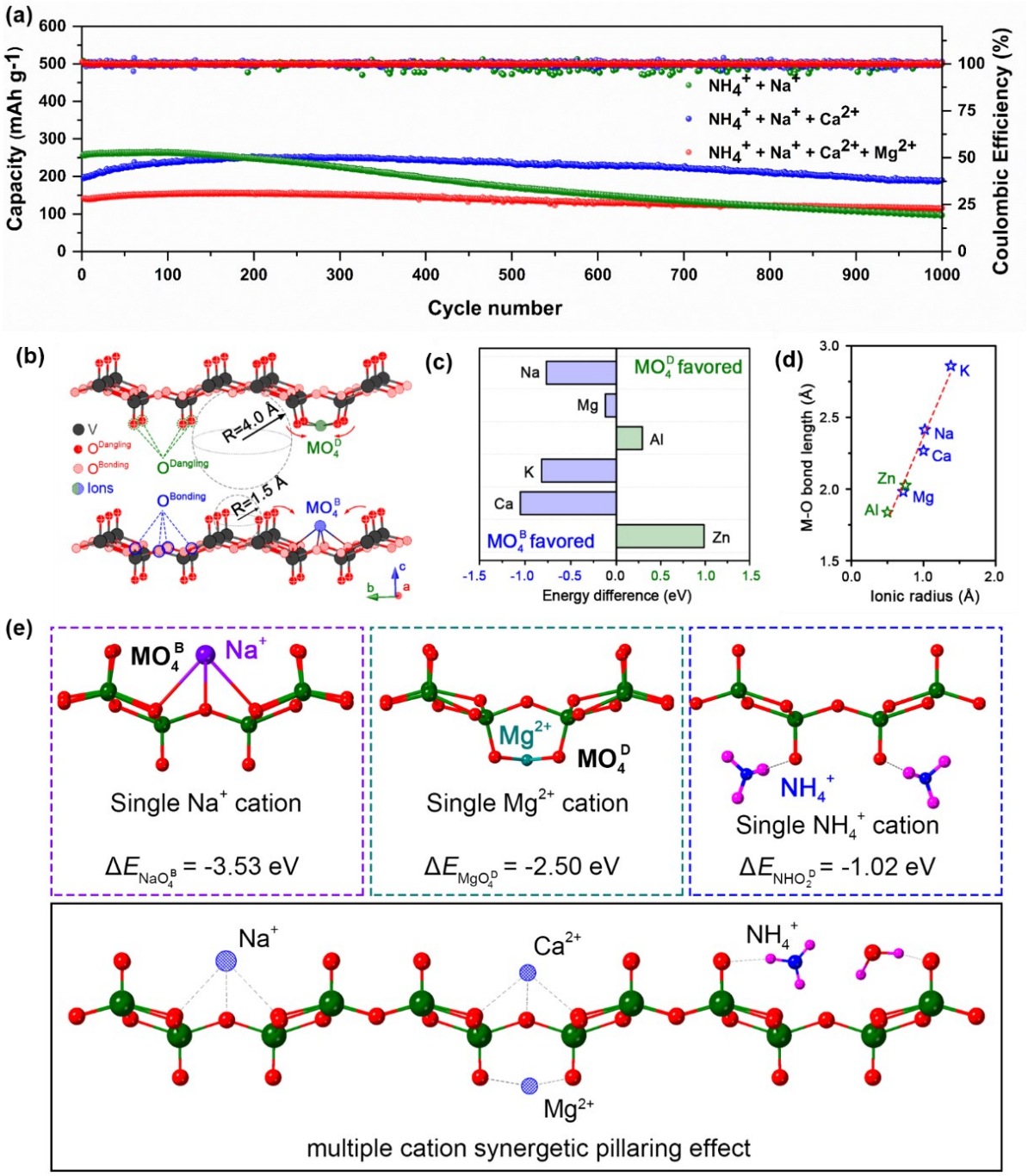

Figure 4. (a) Long-term cycle performance of the cooperative self-assembly products at 0.2 A g^{-1}. **(b)** Atomic scheme of V_2O_5 showing two type of oxygen atoms, the $O^{Bonding}$ (labelled by O^B in blue) in lattice, and $O^{Dangling}$ (labelled by O^D in green) on surface; **(c)** The energy difference calculated by $\Delta E_{\mathrm{diff}} = \Delta E_{\mathrm{MO_4^B}} - \Delta E_{\mathrm{MO_4^D}}$ showing the accommodation site preference of each cation, negative (left) for MO_4^B energetically preferred while positive (right) for MO_4^D energetically preferred. **(d)** The relationship between M-O bond length and ionic radius of studied ions. **(e)** Atomic scheme showing the intercalation of various cations in V_2O_5: Na^+ cation accommodated by forming the MO_4^B bond; Mg^{2+} cation accommodated by forming

the MO_4^D bond; NH_4^+ cation accommodated by forming the MO_2^D bond; and the multiple cation synergetic pillaring effect related with the host of various cations at different accommodation sites.

Zinc ion diffusion kinetic regulation. We further identified the zinc ion diffusion kinetic of this self-assembly series through the galvanostatic intermittent titration technique (GITT) measurement (Figure 5a-b, Figure S19, Supporting Information). Among these samples, K^+-based $M_xV_2O_5{\cdot}nH_2O$ exhibited the highest Zn^{2+} diffusion coefficient of 7.5×10^{-8} cm^2 s^{-1} (platform within 0.9 −1.2 V) and 2.5×10^{-8} cm^2 s^{-1} (platform within 0.4 − 0.8 V). Figure 5c shows the comparison of Zn^{2+} diffusion coefficient in this series with a degressive trend that D_{K+}> D_{Na+} > D_{NH4+} > D_{Ca2+} > D_{Al3+} > D_{Mg2+} > D_{Zn2+} > $D_{bare\ V2O5}$> D_{binary} > $D_{ternary}$ > $D_{quaternary}$. This result indicates that the nanoconfinement of one kind of cation in layered V_2O_5 is beneficial to accelerate zinc-ion transport kinetic. However, further increase of interlayer cations gives rise to the negative influence on the zinc-ion transport. Strikingly, all of the Zn^{2+} diffusion coefficient kinetic in our assembly products is significantly superior to that of $M_xV_mO_n$ based cathode materials reported recently by the conventional hydrothermal route [23-25,43,47-52]. This result identifies that the cation nanoconfinement by this self-assembly strategy would significantly facilitate the rapid transport of zinc ion and result in the larger diffusion coefficient of zinc ion.

The effect of intercalation cation species on the Zn^{2+} diffusion kinetics was further identified in our DFT theoretical simulation. Considering that Mg^{2+}, Al^{3+}, and Ca^{2+} were characterized to be in a high hydrated state for this nanoconfinement and the fundamental role of interlayer water in charge storage for V_2O_5 bilayers has been revealed by Lu et al. recently[53], herein we carried out qualitative discussion on this kinetics effect by selecting Na^+ and K^+-based samples with a much low hydrated state. Figure 5d shows the as-calculated Zn^{2+} diffusion barrier on the pure V_2O_5 single atomic layer without any cation confinement. Surprisingly, a high energy barrier of 1.02 eV was found in this case, indicating a poor mobility of Zn^{2+} in V_2O_5

accompanied by the strong interaction between Zn^{2+} and surrounding O^D atoms. In contrast, the presence of H_2O or NH_4 in the LV space was found to be remarkably favorable for the diffusion behavior, with the barrier declining to 0.87 eV and 0.64 eV for $V_2O_5{\cdot}H_2O$ and $V_2O_5{\cdot}NH_4$, respectively. Figure 5e further illustrates the charge difference density map of V_2O_5 and $K_xV_2O_5$ with Zn ion localed at energetically minimum site during its diffusion. It can be apparently seen in Figure S20 (Supporting Information) that dangling oxygen atoms shift with the presence of K^+ confinement in layered V_2O_5, leading to a weakened hampering effect of Zn ion diffusion by surrounding oxygen atoms. As a result, the distance between each two O^D atoms was prolonged, and the shape of diffusion barrier curve based on the calculated diffusion pathway depecits the maximum energy in the middle of two O^D atoms (red line in Figure 5f), whcih is remarkably differs from that for pure V_2O_5 (Figure 5d). Correspondingly, an obvious reduction in the diffusion energy barrier was observed from initial 1.02 eV (pristine V_2O_5) to 0.89 eV ($Na_xV_2O_5$) and 0.78 eV ($K_xV_2O_5$), which contributeds to the enhanced Zn^{2+} diffusion kinetics by Na^+, K^+ confinement.

Another question is why the Zn^{2+} diffusion kinetics gradually degenerated with the introduction of two or more cations in the V_2O_5 host. The influence of binary cations nanoconfinement was studied by stacking Na^+ and K^+ in one large void space. As confirmed in Figure 5f, such a binary Na^+/ K^+stacking yields to a high diffusion barrier of 1.40 eV, which is remarkably higher than that of unitary Na^+ or K^+ confinement. Accordingly, the nanoconfinement of unitary ions like K^+, Na^+, and NH_4^+ in V_2O_5 framework promotes the mobility of Zn ion with a much declined Zn^{2+} diffusion barrier. However, the further increase the category of intercalation cation to binary or even quarternary system drastically rise the barrier despite of the expanded interlayer distance.

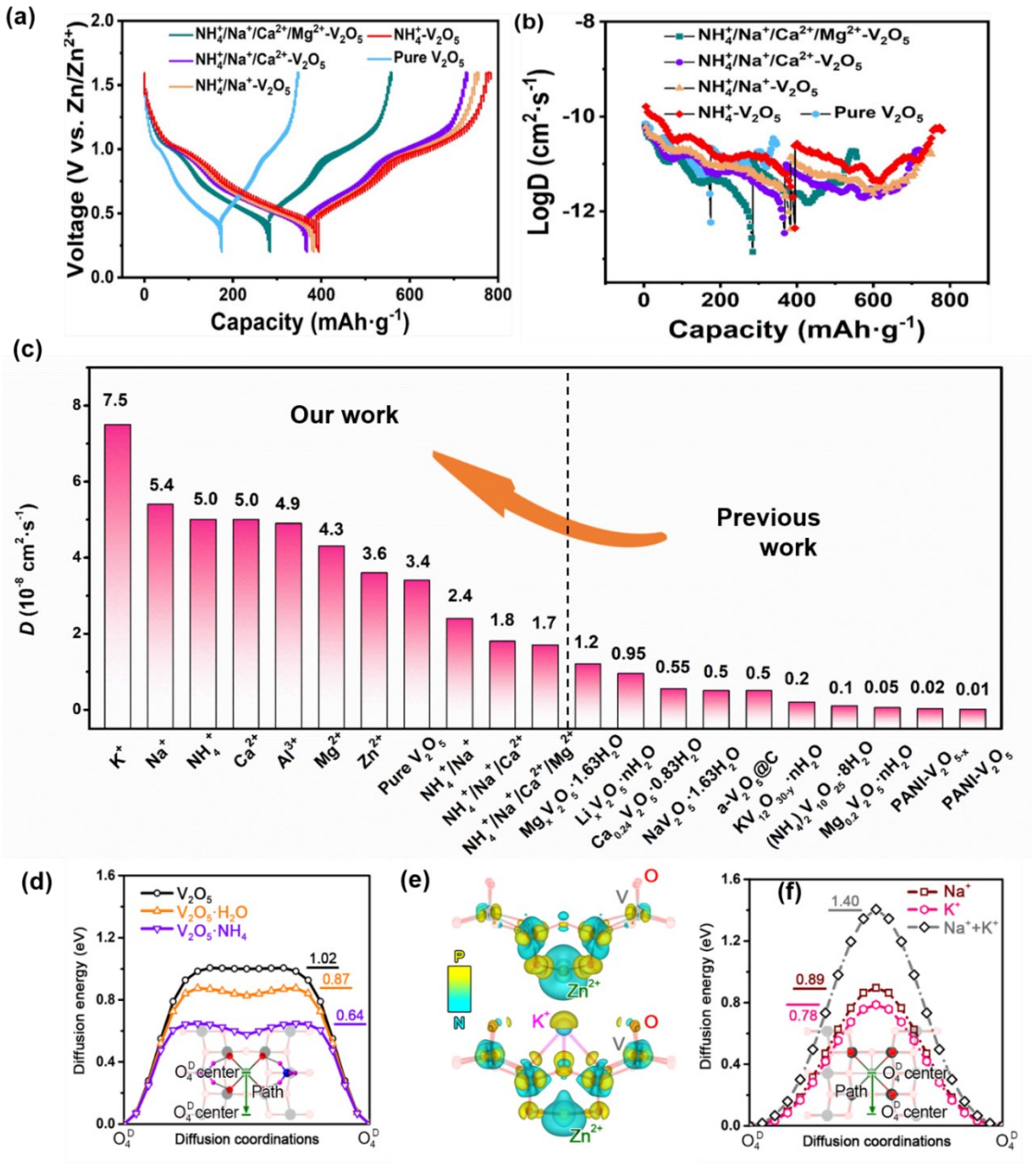

Figure 5. (a-b) GITT analysis of the multiple cation confinement samples by this supramolecular self-assembly. **(c)** Comparison of the Zn^{2+} diffusion coefficient in our assemble series and some previous works [23-25,43,47-52]. **(d)** Comparison of the energy barriers of the Zn^{2+} migration pathways with and without the impacts of H_2O, NH_4 molecules in LV space respectively. **(e)** The mapping of charge difference density demonstrating the bonding property between V_2O_5 and Zn^{2+} ion after K^+ confinement. **(f)** Comparison of the energy barriers of the Zn^{2+} migration pathways with Na^+, K^+ and Na^++ K^+ confinement, respectively.

3. Conclusions

We developed a general, supramolecular self-assembly strategy to nanoconfine unitary cation including NH_4^+, Na^+, K^+, Mg^{2+}, Ca^{2+}, Zn^{2+}, Al^{3+} and multiple cations (NH_4^+ +Na^+, NH_4^+ +Na^+ +Ca^{2+}, NH_4^+ +Na^+ +Ca^{2+}+Mg^{2+}) in ultrathin V_2O_5 nanosheet. We make a systematic comparison on the Zn^{2+} storage capacity, long-term cycling stability, and Zn-ion diffusion kinetics in this self-assemble series. To this end, there are three results which can be concluded from the present study: (1) For the specific capacity: NH_4^+ > binary (NH_4^+ + Na^+) > ternary (NH_4^+ + Na^+ + Ca^{2+}) > Na^+ > Ca^{2+} > Mg^{2+} > quaternary (NH_4^+ + Na^+ + Ca^{2+} + Mg^{2+}) >Zn^{2+} >Al^{3+} > bare V_2O_5; (2) For the capacity retention after long-term cycling: $R_{quaternary} > R_{ternary} > R_{binary}$; (3) For the Zn^{2+} diffusion coefficient: $D_{K+} > D_{Na+} > D_{NH4+} > D_{Ca2+} > D_{Al3+} > D_{Mg2+} > D_{Zn2+} > D_{bare\ V2O5} > D_{binary} > D_{ternary} > D_{quaternary}$. The unitary cation confinement enables a remarkable increase in the Zn^{2+} storage capacity and diffusion kinetics, and the multiple cation confinement gives rise to superior long-term cyclability and structural stability due to multiple cation synergetic pillaring effect. DFT simulation further reveals a declined Zn-ion diffusion barrier by unitary cation nanoconfinement due to a significantly weakened interaction between Zn^{2+} and the dangling oxygen atom of V_2O_5. Our work develops a novel multiple-cations nanoconfinement strategy toward high-performance cathode for aqueous battery, and it also provides new insight into the guest cation regulation of zinc-ion diffusion kinetics and long-term cyclability. Such a supramolecular self-assembly strategy could be extended to the high-entropy materials preparation due to it is facile to introduce various metallic cations into the host frameworks.

Experimental Details

Supramolecular self-assembly. All chemical reagents were used without any purification. In a typical preparation process, 0.3638 g V_2O_5 (99.99%, Sigma Aldrich) was dissolved into 27 mL deionized water. After the addition of 8 mL H_2O_2 (30wt%, Aladdin), the mixture was

stirring for 90 min until a clear claret-red solution was achieved. The above homogenous solution was then transferred into a 50 mL Teflon-lined stainless-steel autoclave and hydrothermally treated at 200 ℃ for 48 h to acquire orange colloid consisted of V_2O_5 nanosheets. Subsequently, the obtained orange V_2O_5 nanosheet colloid was diluted by deionized water and added dropwise to 0.2 mol L^{-1} MCl_x (M refers to Na^+, K^+, Mg^{2+}, Ca^{2+}, Zn^{2+}, Al^{3+}, NH_4^+) solution to realize the colloidal self-assembly procedure along with stirring. The single self-assembly flocculation product was collected after stirring several hours and washed with deionized water for three times. The final product was achieved after drying in vacuum oven at 80 ℃ for 24 h. Cooperative self-assembly was realized by the similar procedure with the dropwise addition of a mixture salt solution (NH_4Cl + NaCl; NH_4Cl + NaCl + $MgCl_2$; NH_4Cl + NaCl + $MgCl_2$ + $CaCl_2$, respectively. 0.2 mol L^{-1} for each cation in the solution) into the V_2O_5 nanosheet colloid.

As a contrast experiment using the conventional hydrothermal route, 0.2 g of V_2O_5 was added to C_2H_5OH and stir until the solution was evenly dispersed, which is designated as solution B. 0.03 g NH_4Cl, 0.03 g NaCl, 0.03 g $CaCl_2$ and 0.03 g $MgCl_2$ were dissolved in deionized water (the volume ratio of ethanol: deionized water was 5:4) to obtain solution C. Then solution C was added to solution B, stir vigorously until the solution is uniformly dispersed. The mixed solution was transferred to a 50 mL autoclave, sealed, and kept at 160°C for 24 hours. After cooling to room temperature, the product was recovered through centrifugation and washed several times with DI water and ethanol.

Materials characterization. The crystal structure characteristics were studied by Ultima IV diffractometer which used Cu Kα radiation (λ = 1.5406 Å). Thermogravimetric (TGA) measurements were carried out using a TG203 F3 instrument in a temperature range of 25 ℃ to 600 ℃ at a heating rate of 5 ℃ min^{-1} under nitrogen atmosphere. Scanning electron microscopy images were generated by FEI 3D field emission scanning electron microscope. Transmission electron microscopy (TEM), selected area electron diffraction (SAED) and

mapping were performed using jem:2100f field emission transmission electron microscope. Inductive coupled plasma (ICP) emission spectrometer was using Agilent 5100 to evaluate metal element ratios. Escalab 250Xi X-ray photoelectron spectroscope system (XPS) was devoted into service for the analysis of element chemical state of the samples, with a C1s peak at 284.8 eV as the standard signal. Layered morphology was investigated by using Shimadzu spm-9700 atomic force microscope. Fourier-transform infrared (FT-IR) and Raman spectroscopies were performed using Bruker TENSOR II infrared spectrometer to analyze and LabRAM HR Evolution spectrometer, respectively.

Electrochemical measurement. The as-prepared $M_xV_2O_5{\cdot}nH_2O$ materials, conductive carbon and polyvinylidene fluoride (PVDF) were mixed at a weight ratio of 7:2:1 with N-methylpyrrolidone (NMP) as a solution to make a homogeneous slurry. It was pasted onto stainless steel slice and dried in vacuum atmosphere at 60 ℃. The cells were assembled with the as-prepared materials as cathode, zinc foils as anode, Whatman GF/D glass fibers as separator and 2.0 M $Zn(OTf)_2$ aqueous solution (Alfa) as electrolyte. The cyclic voltammetry (CV) tests and electrochemical impedance spectroscopy (EIS) were studied on the electrochemical workstation CHI660E. Galvanostatic charge-discharge (GCD) was tested on a LANDdt battery tester system (China). GITT was applied to investigate the diffusion kinetics for Zn^{2+} in different $M_xV_2O_5{\cdot}nH_2O$.

Calculation method: The modeling in this work was performed in the framework of Density Functional Theory (DFT) as implemented in the Vienna *Ab initio* Simulation Package (VASP). The Projector Augmented Wave (PAW) method was adopted to solve the Kohn-Sham equations, and the Generalized Gradient Approximation constructed by Perdew-Burke-Ernzerhof (GGA-PBE) was taken for exchange-correlation functional. All the investigated structures in this work were fully relaxed at the cutoff energy of 480 eV in a Γ-centered k-grid scheme with a total number of 40, during which process the convergence criteria were set to be 10^{-4} eV for energy and 10^{-2} eV/Å for force. The monolayer V_2O_5 was constructed based on the

optimized bulk V_2O_5, by setting a lattice parameter *c* of 11.0 Å according to the XRD characterization results. Thereafter, the intercalation/absorption of ions (Na, Mg, Al, K, Ca, Zn) and molecules (H_2O, NH_4) on the V_2O_5 monolayer was investigated by computing the formation energy, and the accommodation site preference of each cation was then revealed by calculating the energy difference, according to $\Delta E_{\mathrm{diff}} = \Delta E_{\mathrm{MO_4^B}} - \Delta E_{\mathrm{MO_4^D}}$, in which $\Delta E_{\mathrm{MO_4^B}}$ refers to the intercalation energy of M cation on V_2O_5 while forming MO_4^B bonds, and $\Delta E_{\mathrm{MO_4^D}}$ refers to the intercalation energy of M cation on V_2O_5 while forming MO_4^D bonds.

Supporting Information

Supporting Information is available from the Wiley Online Library or from the author.

Acknowledgments

This work was financially supported by the National Natural Science Foundation of China (52171203 and 52371214), the Natural Science Foundation of Jiangsu Province (Grant No. BK20211516), the National Key Research and Development Program of China (Grant No. 2021YFB2400400), the Jiangsu Province Excellent Post-Doctoral Program (2022ZB77), and the Fundamental Research Funds for the Central Universities (2242023K5001).

Conflicts of Interest

The authors declare no conflict of interest.

Reference

[1] R. F. Service. *Science* 2021, 372, 890.

[2] Y. L. Liang, H. Dong, D. Aurbach, Y. Yao. *Nat. Energy* 2020, 5, 646.

[3] Y. Kim, Y. Park, M. Kim, J. Lee, K. J. Kim, J. W. Choi. *Nat. Commun.* 2022, 13, 2371.

[4] Z. D. Zhao, R. Wang, C. X. Peng, W. J. Chen, T. Q. Wu, B. Hu, W. J. Weng, Y. Yao, J. X. Zeng, Z. H. Chen, P. Y. Liu, Y. C. Liu, G. S. Li, J. Guo, H. B. Lu, Z. P. Guo. *Nat. Commun*. 2021, 12, 6606.

[5] S. Jin, Y. Q. Shao, X. S. Gao, P. Y. Chen, J. X. Zheng, S. F. Hong, J. F. Yin, Y. L. Joo, L. A. Archer. *Sci. Adv.* 2022, 8, 4456.

[6] L. Ma, M. A. Schroeder, O. Borodin, T. P. Pollard, M. S. Ding, C. S. Wang, K. Xu. *Nat. Energy* 2022, 5, 743.

[7] L. L. Wang, K. W. Huang, J. T. Chen, J. R. Zheng. *Sci. Adv.* 2019, 5, 4279.

[8] H. B. Dong, J. W. Li, J. Guo, F. L. Lai, F. J. Zhao, Y. D. Jiao, D. J. L. Brett, T. X. Liu, G. J. He, L. P. Parkin. *Adv. Mater.* 2021, 33, 2007548.

[9] Y. Liu, J. Wang, Y. X. Zeng, J. Liu, X. Q. Liu, X. H. Lu. *Small* 2020, 16, 1907458.

[10] H. F. Liang, Z. Cao, F. W. Ming, W. L. Zhang, D. H. Anjum, Y. Cui, L. Cavallo, H. N. Alshareef. *Nano Lett.* 2019, 19, 3199.

[11] W. S. V. Lee, T. Xiong, X. P. Wang, J. M. Xue. *Small Methods* 2021, 5, 2000815.

[12] H. L. Pan, Y. Y. Shao, P. F. Yan, Y. W. Cheng, K. S. Han, Z. M. Nie, C. M. Wang, J. H. Yang, X. L. Li, P. Bhattacharya, K. T. Mueller, J. Liu. *Nat. Energy* 2016, 1, 1-7.

[13] X. L. Zhou, K. X. Ma, Q. Y. Zhang, G. Z. Yang, C. X. Wang. *Nano Research* 2022, 15, 8039.

[14] S. S. Zhang, Z. J. Liu, L. Li, S. K. Li, S. Q. Zhang, Y. D. Tang, J. L. Yu, H. Y. Zhang. *Chem. Commun.* 2021, 57, 10339.

[15] L. T. Ma, S. M. Chen, C. B. Long, X. L. Li, Y. W. Zhao, Z. X. Liu, Z. D. Huang, B. B. Dong, J. A. Zapien, C. Y. Zhi. *Adv. Energy Mater.* 2019, 9, 1902446.

[16] S. Islam, M. H. Alfaruqi, V. Mathew, J. J. Song, S. J. Kim, S. Kim, J. Jo, J. P. Baboo, D. T. Pham, D. Y. Putro, Y. K. Sun, J. K. Kim. *J. Mater. Chem. A* 2017, 5, 23299.

[17] M. H. Alfaruqi, V. Mathew, J. Gim, S. J. Kim, J. J. Song, J. P. Baboo, S. H. Choi, J. Kim. *Chem. Mater*. 2015, 27, 3609.

[18] B. K. Wu, G. B. Zhang, M. Y. Yan, T. F. Xiong, P. He, L. He, X. Xu, L. Q. Mai. *Small* 2018, 14, 1703850.

[19] Z. Liu, G. Pulletikurthi, F. Endres. *ACS Appl. Mater. Inter*. 2016, 8, 12158.

[20] R. Trocoli, F. L. Mantia. *ChemSusChem* 2015, 8, 481.

[21] L. Y. Zhang, L. Chen, X. F. Zhou, Z. P. Liu. *Adv. Energy Mater.* 2015, 5, 1400930.

[22] R. F. Service. *Science* 2018, 362, 508.

[23] S. C. Liu, H. Zhu, B. H. Zhang, G. Li, H. K. Zhu, Y. Ren, H. B. Geng, Y. Yang, Q. Liu, C. C. Li. *Adv. Mater.* 2020, 32, 2001113.

[24] W. J. Li, C. Han, Q. F. Gu, S. L. Chou, J. Z. Wang, H. K. Liu, S. X. Dou. *Adv. Energy Mater*. 2020, 10, 2001852.

[25] Y. Q. Yang, Y. Tang, G. Z. Fang, L. T. Shan, J. S. Guo, W. Y. Zhang, C. Wang, L. B. Wang, J. Zhou, S. Q. Liang. *Energy & Environ. Sci.* 2018, 11, 3157.

[26] C. Xia, J. Guo, P. Li, X. X. Zhang, H. N. Alshareef. *Angew. Chem. Int. Ed.* 2018, 57, 4007.

[27] T. T. Lv, G. Y. Zhu, S. Y. Dong, Q. Q. Kong, Y. Peng, S. Jiang, G. X. Zhang, Z. L. Yang, S. Y. Yang, X. C. Dong, H. Pang, Y. Z. Zhang. *Angew. Chem. Int. Ed.* 2023, 62, 202216089.

[28] L. F. Hu, Z. Y. Wu, C. J. Lu, F. Ye, Q. Liu, Z. M. Sun. *Energy & Environ. Sci.* 2021, 14, 4095.

[29] R. Li, F. Xing, T. Y. Li, H. M. Zhang, J. W. Yan, Q. Zheng, X. F. Li. *Energy Storage Mater.* 2021, 38, 590.

[30] L. Z. Wang, K. Takada, A. Kajiyama, M. Onoda, Y. Michiue, L. Q. Zhang, M. Watanabe, T. Sasaki. *Chem. Mater.* 2003, 15, 4508.

[31] R. Z. Ma, X. H. Liu, J. B. Liang, Y. Bando, T. Sasaki. *Adv. Mater.* 2014, 26, 4173.

[32] P. Xiong, B. Sun, N. Sakai, R. Z. Ma, T. Sasaki, S. J. Wang, J. Q. Zhang, G. X. Wang. *Adv. Mater.* 2020, 32, 1902654.

[33] S. Y. Dong, W. Shin, H. Jiang, X. Y. Wu, Z. F. Li, J. Holoubek, W. F. Stickle, B. Key, C. Liu, J. Lu, P. A. Greaney, X. G. Zhang, X. L. Ji. *Chem* 2019, 5, 1537.

[34] T. Sasaki, M. Watanabe, H. Hashizume, H. Yamada, H. Nakazawa. *Am. Chem. Soc.* 1996, 118, 8329

[35] X. Lu, Y. Zhang, J. Zheng, H. Jiang, T. Hu, C. G. Meng. *J. Am. Chem. Soc.* 2007, 129,

8000.

[36] C. C. Torardi, C. R. Miao, M. E. Lewittes, Z. Li. *Angew. Chem. Int. Ed.* 2019, 58, 7062.

[37] Z. P. Liu, R. Z. Ma, M. Osada, K. Takada, T. Sasaki. *J. Am. Chem. Soc.* 2005, 127, 13869.

[38] N. Lv, R. Q. Ren, Y. L. Wu, Z. K. Xu, D. X. Wu, X. Y. You, G. Y. Zhu, Y. Z. Zhang, S. Y. Dong. *Electrochim. Acta* 2022, 431, 141097.

[39] Y. Gogotsi, R. M. Penner. *ACS Nano* 2018, 12, 2081-2083.

[40] V. Augustyn, J. Come, M. A. Lowe, J. W. Kim, P. L. Taberna, S. H. Tolbert, H. D. Abruna, P. Simon, B. Dunn. *Nat. Mater.* 2013, 12, 518.

[41] X. Liu, H. Zheng, D. Geiger, J. Han, A. Varzi, U. Kaiser, A. Moretti, S. Passerini. *Chem. Commun.* 2019, 55, 2265.

[42] W. J. Zhou, J. Z. Chen, M. F. Chen, A. R. Wang, A. X. Huang, X. W. Xu, J. L. Xu, C. P. Wong. *J. Mater. Chem. A* 2020, 8, 8397.

[43] P. Hu, T. Zhu, X. P. Wang, X. J. Wei, M. Y. Yan, J. T. Li, W. Luo, W. C. Zhang, L. Zhou, Z. Q. Zhou, L. Q. Mai. *Nano Lett.* 2018, 18, 1758.

[44] Y. Q. Fan, Z. X. Qu, W. T. Zhong, Z. W. Hu, H. A. Younus, C. H. Yang, X. W. Wang, S. G. Zhang. *ACS Appl. Mater. Inter.* 2021, 13, 7377.

[45] P. He, M. Y. Yan, X. B. Liao, Y. Z. Luo, L. Q. Mai, C. W. Nan. *J. Mater. Chem. A* 2019, 7, 20806.

[46] B.Y. Tang, L.T. Shan, S.Q. Liang, J. Zhou. *Energy Environ. Sci.* 2019, 12, 3291

[47] T. Meng, C. F. Liu, J. Q. Zheng, X. X. Jia, E. P. Jahrman, G. T. Seidler, D. H. Long, M. Atif, M. Alsalhi, G. Z. Cao. *Energy Storage Mater.* 2020, 29, 9.

[48] F. W. Ming, H. F. Liang, Y. J. Lei, S. Kandambeth, M. Eddaoudi, H. N. Alshareef. *ACS Energy Lett.* 2018, 3, 2602.

[49] C. Xia, J. Guo, P. Li, X. X. Zhang, H. N. Alshareef. *Angew. Chem. Int. Ed.* 2018, 57, 3943.

[50] S. Z. Deng, Z. S. Yuan, Z. W. Tie, C. D. Wang, L. Song, Z. Q. Niu. *Angew. Chem. Int. Ed.* 2020, 59, 22002.

[51] T. Y. Wei, Q. Li, G. Z. Yang, C. X. Wang. *J. Mater. Chem. A*, 2018, 6, 20402.

[52] J. D. Guan, L. Y. Shao, L. Yu, S. G. Wang, X. Y. Shi, J. J. Cai, Z. P. Sun. *Chem. Eng. J.* 2022, 443, 136502.

[53] G. X. Liu, H. W. Huang, R. Bi, X. Xiao, T. Y. Ma, L. Zhang. *Adv. Energy Mater.* 2023, 13, 2202515.

Table of contents

A general, supramolecular self-assembly strategy was developed to intercalate unitary cation including NH_4^+, Na^+, K^+, Mg^{2+}, Ca^{2+}, Zn^{2+}, Al^{3+} and multiple cations (NH_4^+ +Na^+, NH_4^+ +Na^+ +Ca^{2+}, NH_4^+ +Na^+ +Ca^{2+}+Mg^{2+}) in ultrathin V_2O_5 nanosheets. The success on multiple cations nanoconfinement enables very fast zinc ion diffusion kinetics and excellent long-term cycling stability. The optimized diffusion coefficient of zinc ion (7.5×10^{-8} cm^2 s^{-1}) in this assembly series surpasses most of the V-based cathodes reported up to date.

Keywords： V_2O_5 nanosheets; supramolecular assembly; nanoconfinement; multiple cations; aqueous zinc-ion battery

Multiple Cations Nanoconfinement in Ultrathin V_2O_5 Nanosheets Enables Ultrafast Ion Diffusion Kinetics toward High-performance Zinc Ion Battery

*Yang Liu, Chengjie Lu, Yunting Yang, Wenshu Chen, Fei Ye, Hongliang Dong, Yuping Wu, Renzhi Ma, Linfeng Hu**

ToC figure

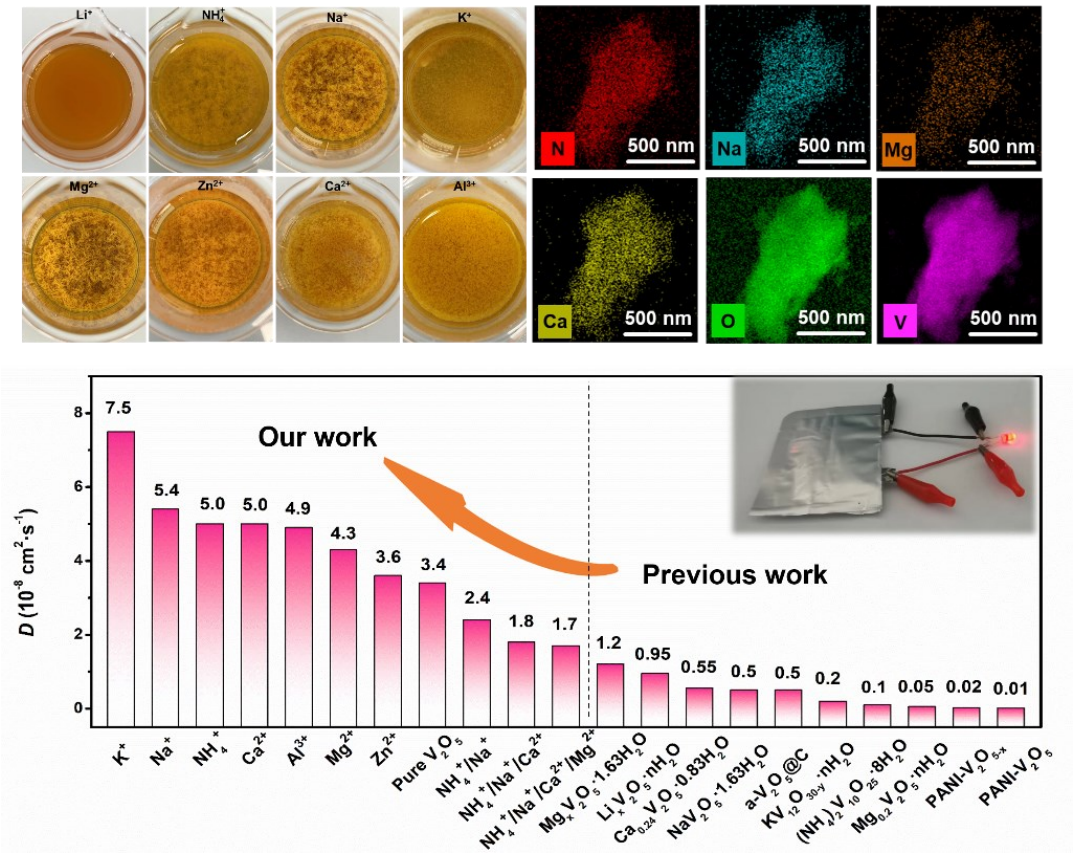

Supporting Information

Multiple Cations Nanoconfinement in Ultrathin V_2O_5 Nanosheets Enables Ultrafast Ion Diffusion Kinetics toward High-performance Zinc Ion Battery

*Yang Liu, Chengjie Lu, Yunting Yang, Wenshu Chen, Fei Ye, Hongliang Dong, Yuping Wu, Renzhi Ma, Linfeng Hu**

[*] Prof. L. F. Hu, W.S. Chen, Y. Liu, Y. T. Yang, C. J. Lu, F. Ye,

School of Materials Science and Engineering, Southeast University

Nanjing, 211189, P. R. China

These authors contributed equally: Y. Liu, Dr. C. J. Lu

*Email: linfenghu@seu.edu.cn

Dr. H. L. Dong

Center for High Pressure Science and Technology Advanced Research, Shanghai, 201203, P. R. China

Prof. Y. P. Wu

School of Energy and Environment, Southeast University, Nanjing 211189, P. R. China

Prof. R. Z. Ma

Research Center for Materials Nanoarchitectonics, National Institute for Materials Science (NIMS), Namiki 1-1, Tsukuba, Ibaraki 305-0044, Japan.

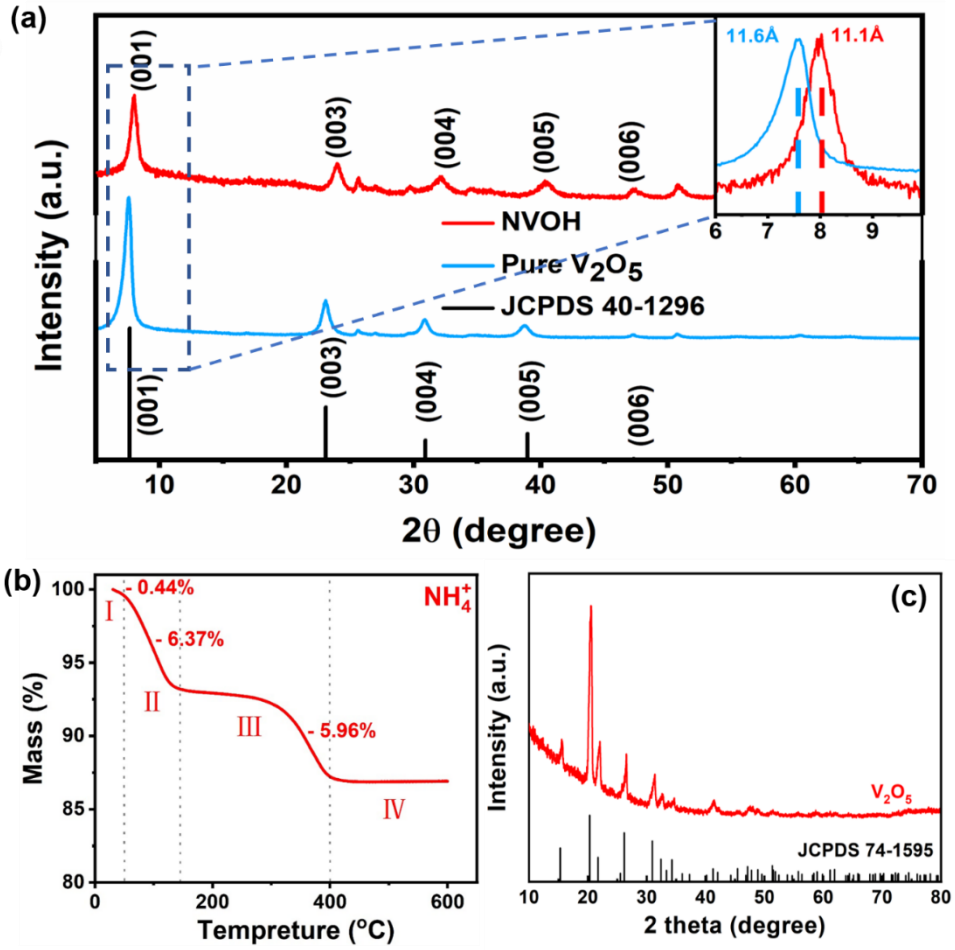

Figure S1. (a) XRD patterns of the as-assembled $(NH_4)_{0.77}V_2O_5 \cdot 0.8H_2O$ and freeze dried V_2O_5 nanosheets. (i) TGA analysis of $(NH_4)_{0.77}V_2O_5 \cdot 0.8H_2O$. (c) XRD pattern of the annealed sample after 400°C, 2h heating of $(NH_4)_{0.77}V_2O_5 \cdot 0.8H_2O$.

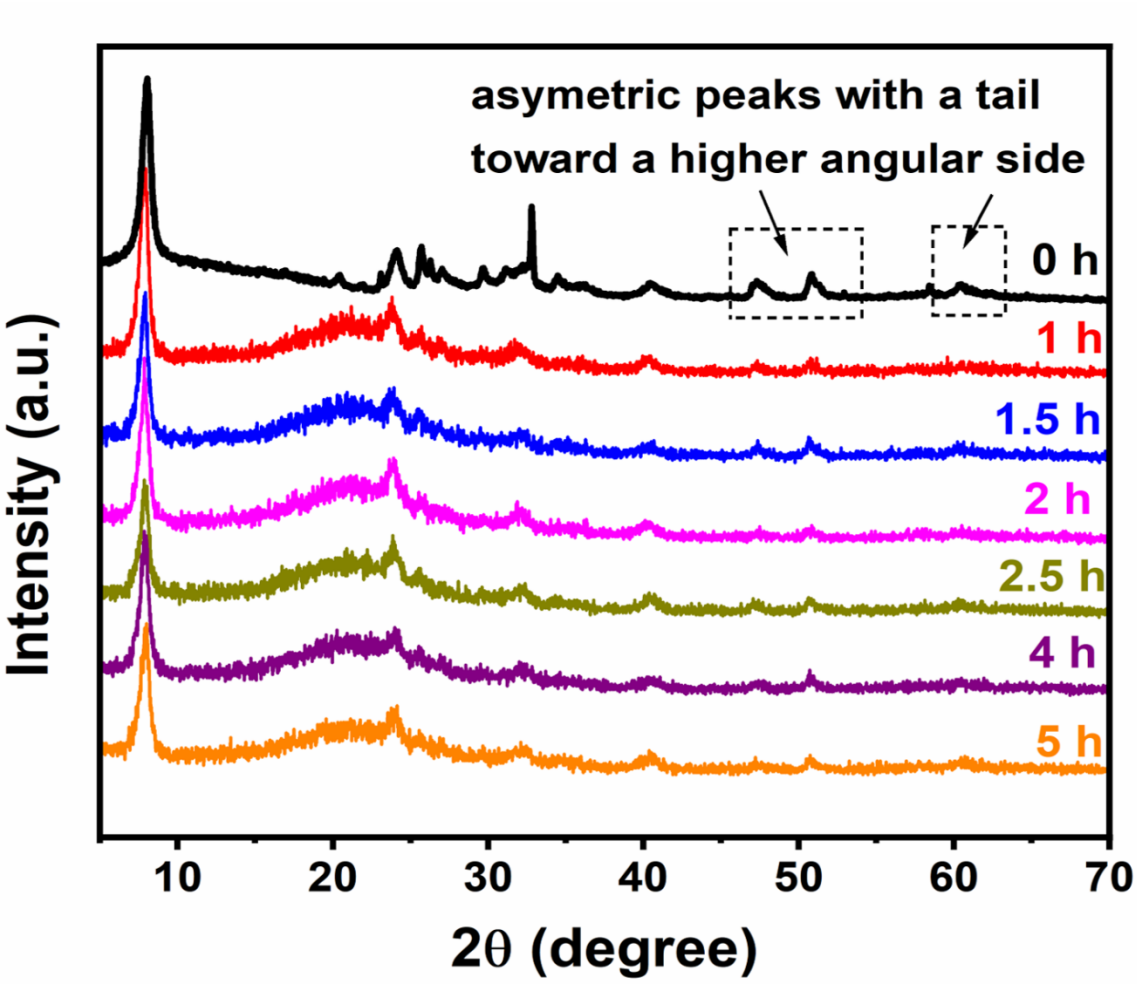

Figure S2. XRD patterns of the NH_4^+ self-assembled samples at various aging time.

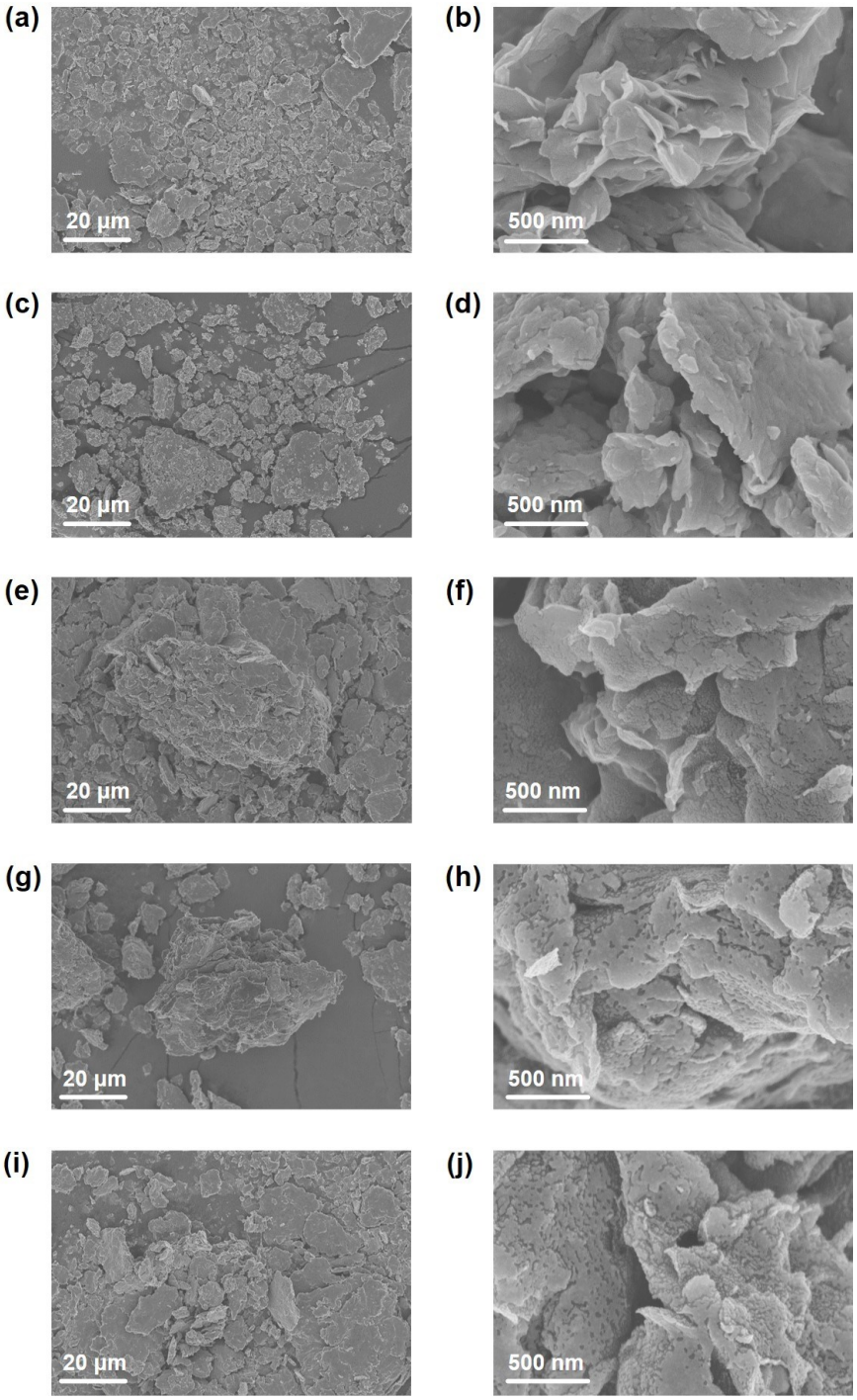

Figure S3. Morphology of $(NH_4)_{0.77}V_2O_5{\cdot}0.8H_2O$ at various aging times. SEM images of the as-prepared $(NH_4)_{0.77}V_2O_5{\cdot}0.8H_2O$ at various aging times: **(a, b)** 1 h; **(c, d)** 1.5 h; **(e, f)** 2 h; **(g, h)** 4 h; **(i, j)** 5 h. The surface of the sample aging at 1.0 h exhibits restacked sheet morphology with very smooth surface. With prolonging the aging time, the surface generally converted to rather rough and porous.

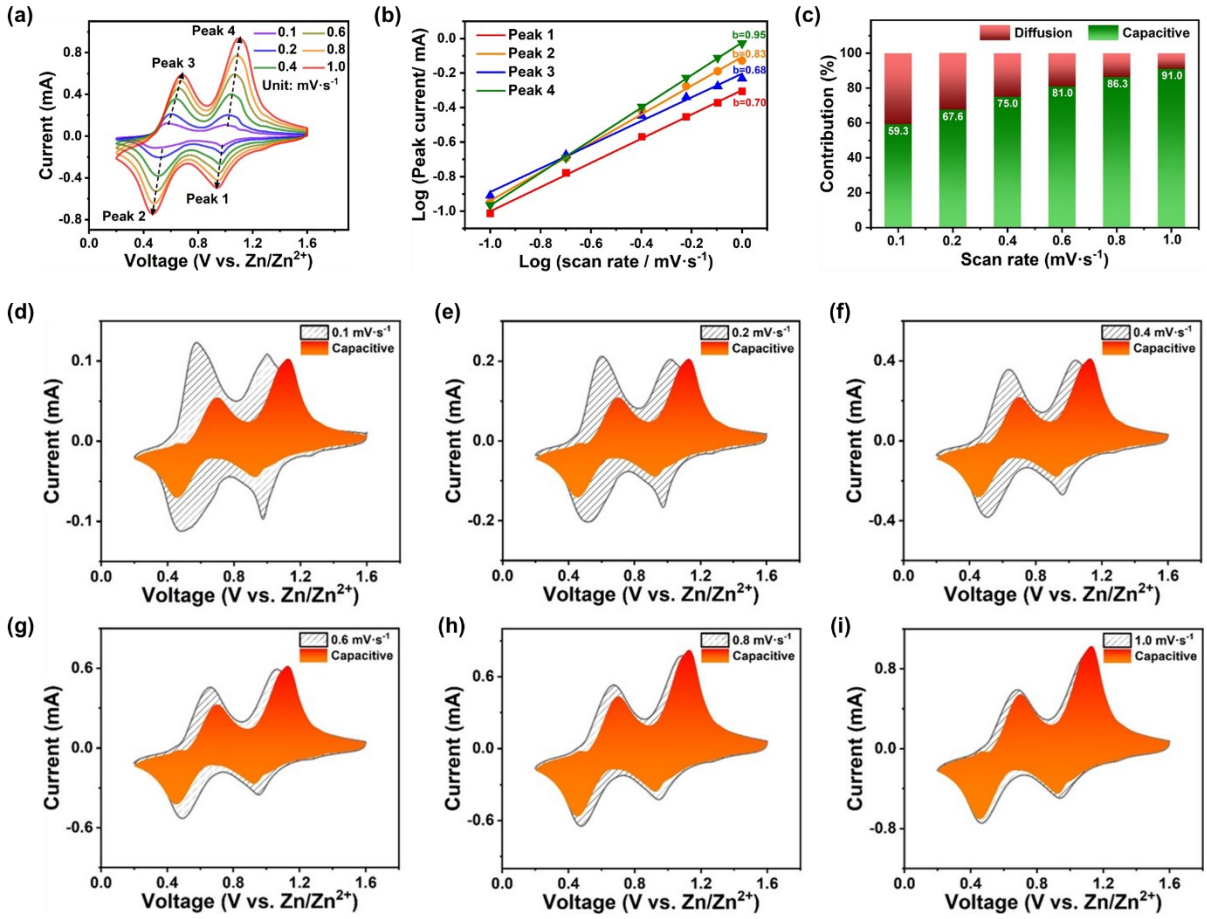

Figure S4. Capacity contribution type analysis of $(NH_4)_{0.77}V_2O_5{\cdot}0.8H_2O$. (a) CV curves at various scan rates. **(b)** The as-calculated *b* value of four different peaks 1-4. The *b* value of 0.70, 0.83, 0.68 and 0.95 can be derived for the peak 1 to peak 4 of the four primary peaks, respectively, indicating capacitive-effect is the predominant contribution for Zn-ion storage. **(c)** Capacitive and diffusion contribution bar graph calculated from the dependence of peak current density and the scan rate. CV curves containing the schematic of capacitive contribution of $(NH_4)_{0.77}V_2O_5{\cdot}0.8H_2O$ at the current density of **(d)** 0.1, **(e)** 0.2, **(f)** 0.4, **(g)** 0.6, **(h)** 0.8 and **(i)** 1.0 $mV{\cdot}s^{-1}$, respectively. In general, the peak current density and the corresponding scan rate in a specialized CV curve obey the following relationship:

$$i = a\,v^b$$

where *a* and *b* are variable values due to the capacity contribution type. A *b* value of 0.5 implies a semi-infinite diffusion mechanism, while a *b* value of 1.0 indicates predominant capacitive behavior. For our $(NH_4)_{0.77}V_2O_5{\cdot}0.8H_2O$ cathode, the *b* value of 0.70, 0.83, 0.68, and 0.95 can be derived for the peak 1 to peak 4 of the four primary peaks, respectively, indicating capacitive-effect is the predominant contribution for Zn-ion storage.

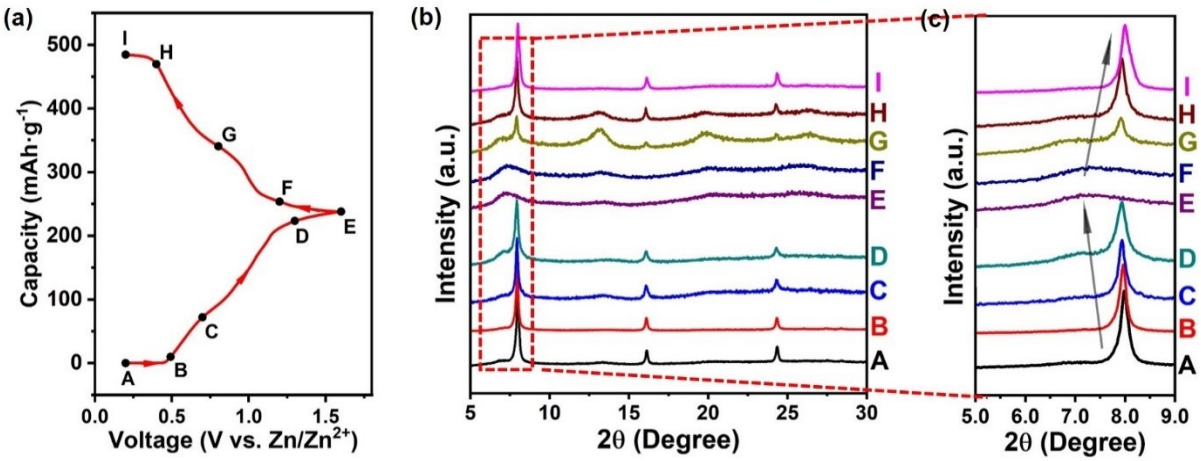

Figure S5. *Ex situ* XRD patterns of the as-assembled $(NH_4)_{0.77}V_2O_5 \cdot 0.8H_2O$ cathode. The (001) diffraction peak shifts gradually from 7.98° towards a smaller diffraction angle during the discharging process, implying an increment in the interlayer distance due to the intercalation of Zn^{2+}. Besides, the (001) diffraction peak returned to its original state during the charging process, demonstrating the extraction process of Zn^{2+} without the destruction of initial layered structure.

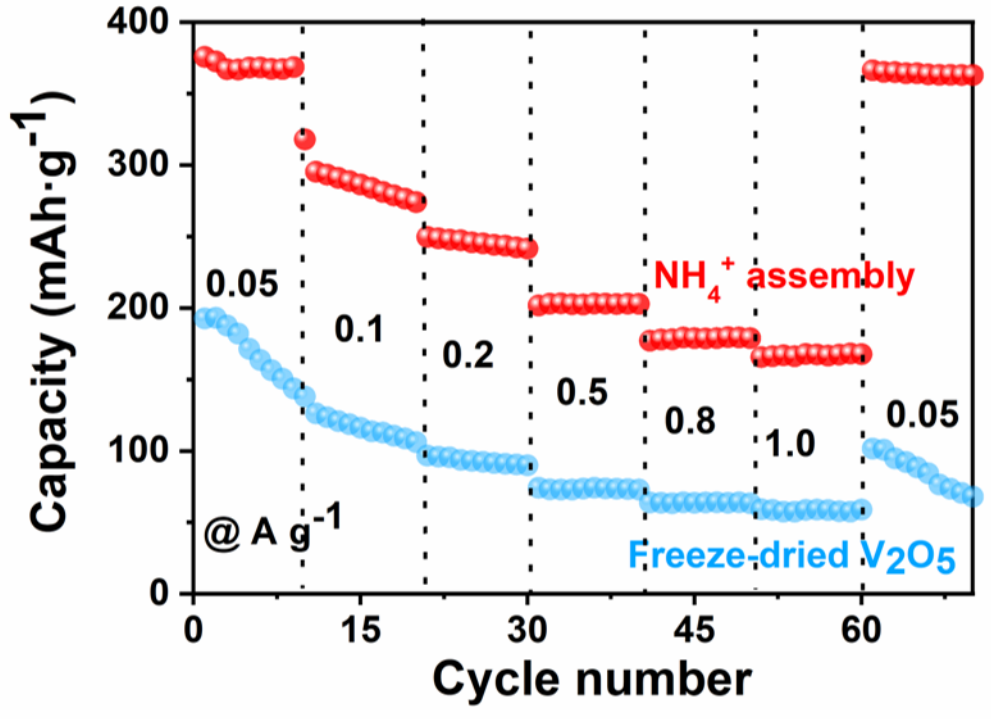

Figure S6. Rate-performance of the $(NH_4)_{0.77}V_2O_5 \cdot 0.8H_2O$ sample.

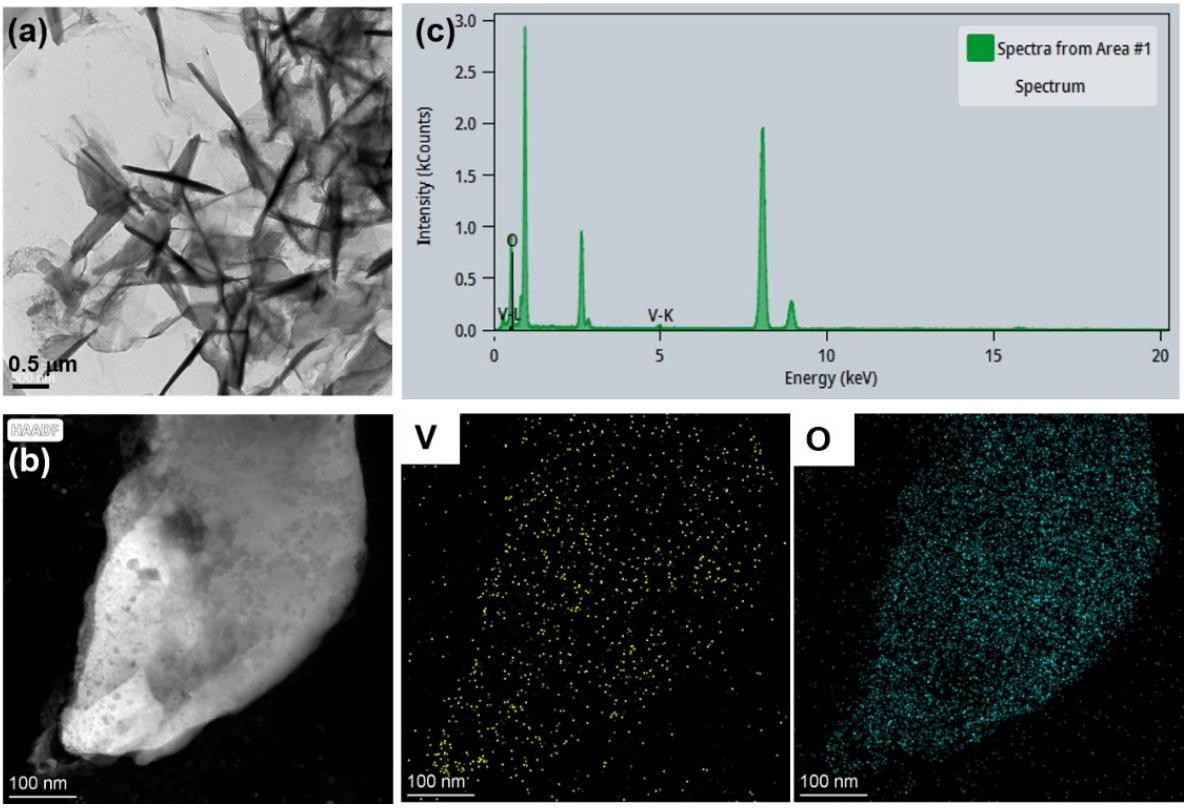

Figure S7. TEM observation of the assemble product after the addition of Li-salt into the V_2O_5 nanosheet suspension.

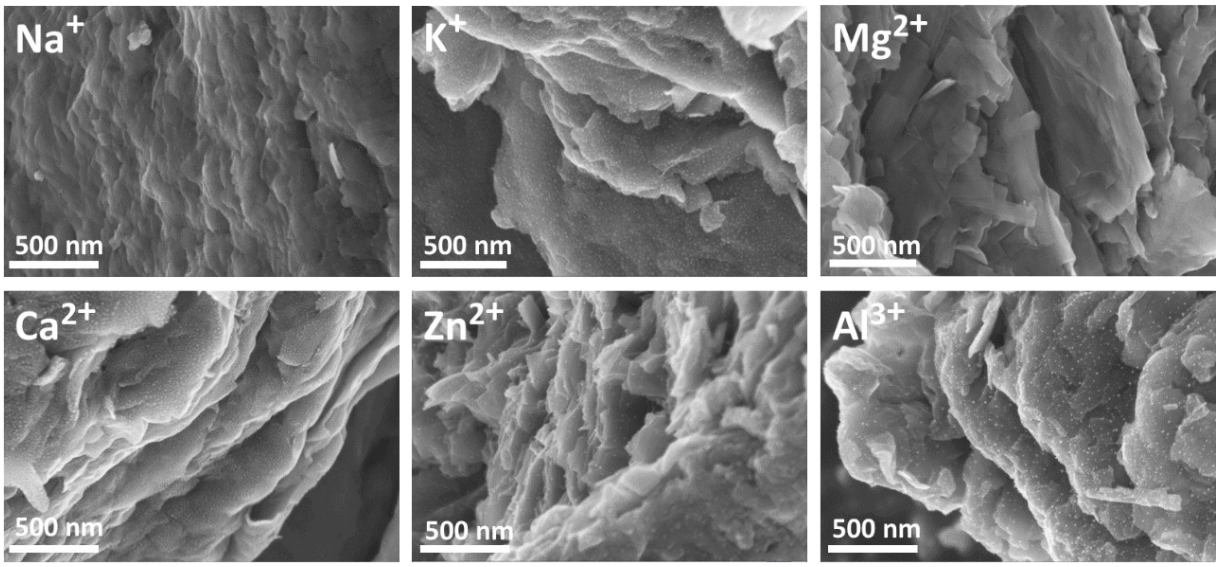

Figure S8. SEM images of $M_xV_2O_5{\cdot}nH_2O$ (M: Na^+, K^+, Mg^{2+}, Ca^{2+}, Zn^{2+}, Al^{3+}) series by the supramolecular self-assembly.

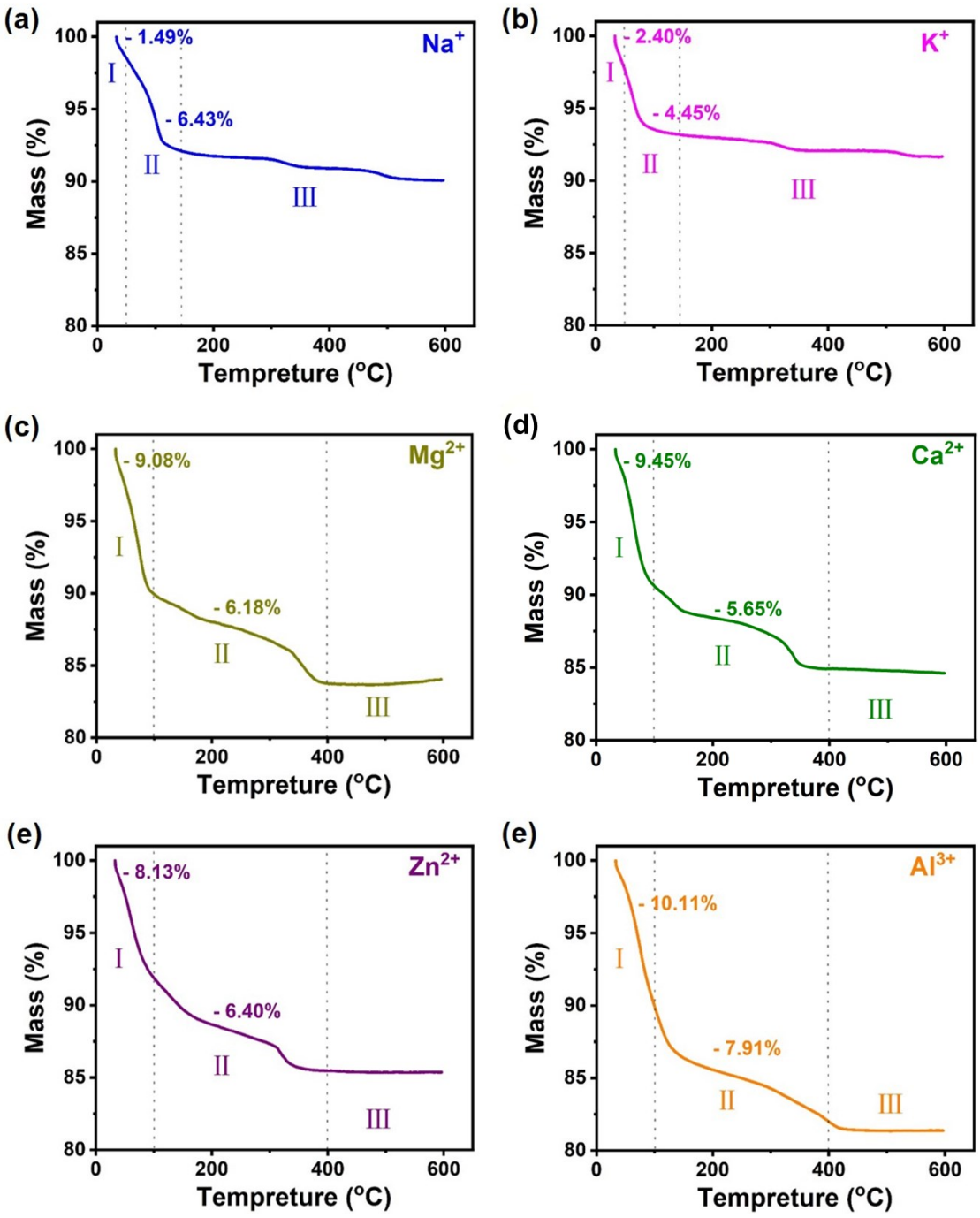

Figure S9. TGA analysis of patterns of the $M_xV_2O_5{\cdot}nH_2O$ assemble products. The TGA analysis of $M_xV_2O_5{\cdot}nH_2O$ (M refers to Na^+, K^+, Mg^{2+}, Ca^{2+}, Zn^{2+}, Al^{3+}) nanosheet, which can be identified as **(a)** $Na_{0.34}V_2O_5{\cdot}0.46H_2O$, **(b)** $K_{0.30}V_2O_5{\cdot}0.16H_2O$, **(c)** $Mg_{0.16}V_2O_5{\cdot}0.82H_2O$, **(d)** $Ca_{0.14}V_2O_5{\cdot}0.72H_2O$, **(e)** $Zn_{0.29}V_2O_5{\cdot}0.83H_2O$ and **(f)** $Al_{0.19}V_2O_5{\cdot}1.19H_2O$, respectively.

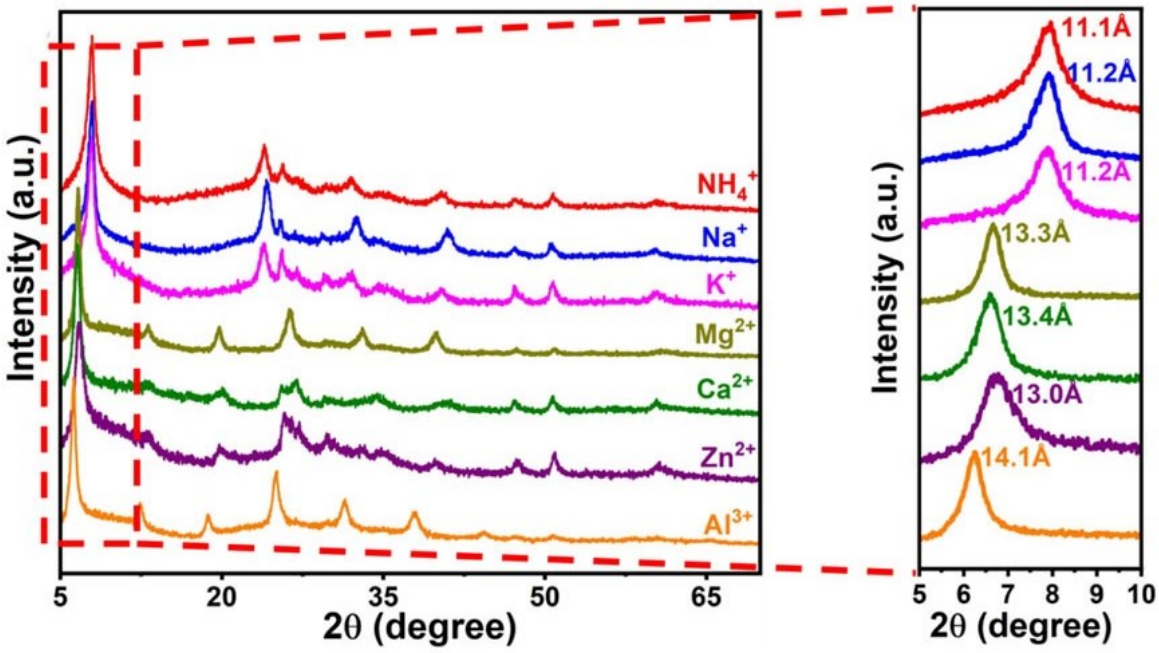

Figure S10. XRD patterns of the Na^+, K^+, Mg^{2+}, Ca^{2+}, Zn^{2+}, Al^{3+}-based $M_xV_2O_5{\cdot}nH_2O$.

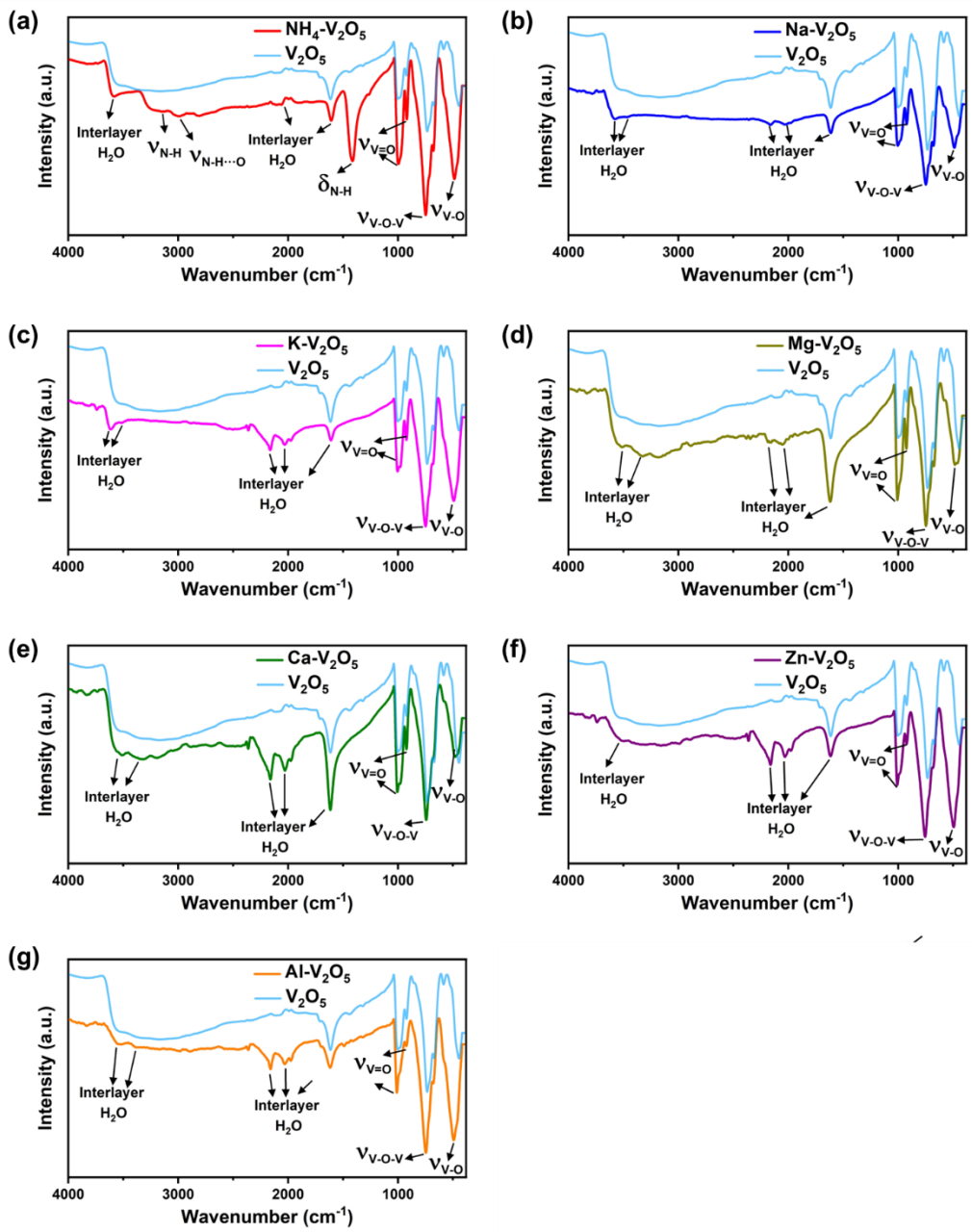

Figure S11. FITR spectra of the as-prepared $(NH_4)_{0.77}V_2O_5{\cdot}0.8H_2O$. The absorption peaks located at 3151 and 1451 cm^{-1}, which can be ascribed to the stretching vibration and bending vibration mode of N-H bond of NH_4^+ group, respectively. Moreover, the absorption peak located at 2998 cm^{-1} is attributed to the stretching vibration mode of dissociated N-H···O bond, suggesting that the interlayer NH_4^+ cation is connected to the V_2O_5 host layer by hydrogen bonding. In addition, the characteristic peaks located at 3581 and 1606 cm^{-1} confirm the existence of interlayer crystal water in the flocculation product.

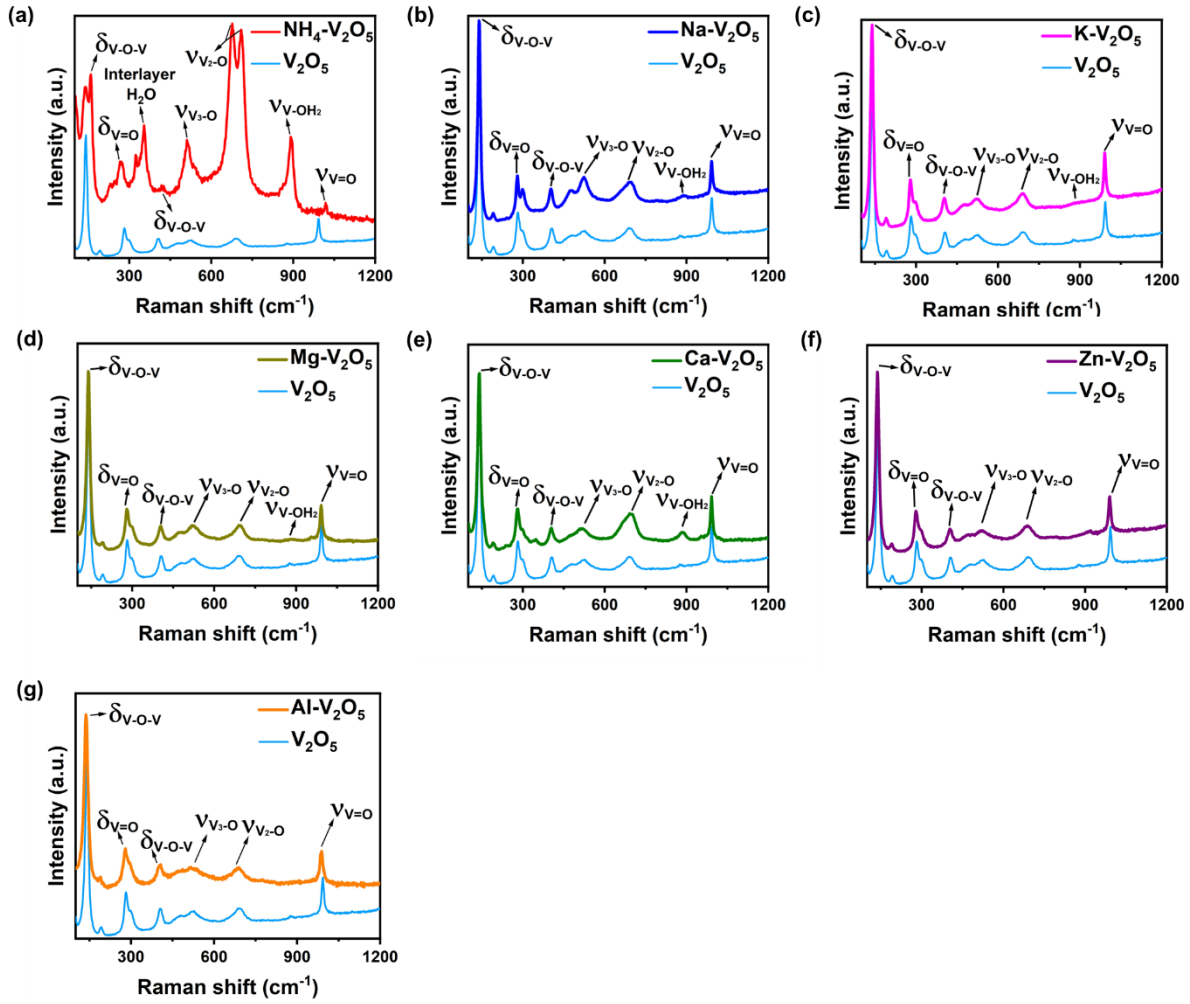

Figure S12. Raman spectra of the $(NH_4)_{0.77}V_2O_5{\cdot}0.8H_2O$ by the supramolecular self-assembly. The characteristic peaks at 1018 cm^{-1} and 271 cm^{-1} are assigned to the terminal oxygen (V=O) stretching mode and bending vibration, respectively. The characteristic peaks of the bending vibration of V-O-V chains can be detected at 159 and 417 cm^{-1}. Two obviously characteristic peaks at 676 and 709 cm^{-1} are assigned to disordered stretching vibration of V_2-O (doubly coordinated oxygen) bonds, and the peak at 516 cm^{-1} originates from the stretching vibration of V_3-O (triply coordinated oxygen) bonds.

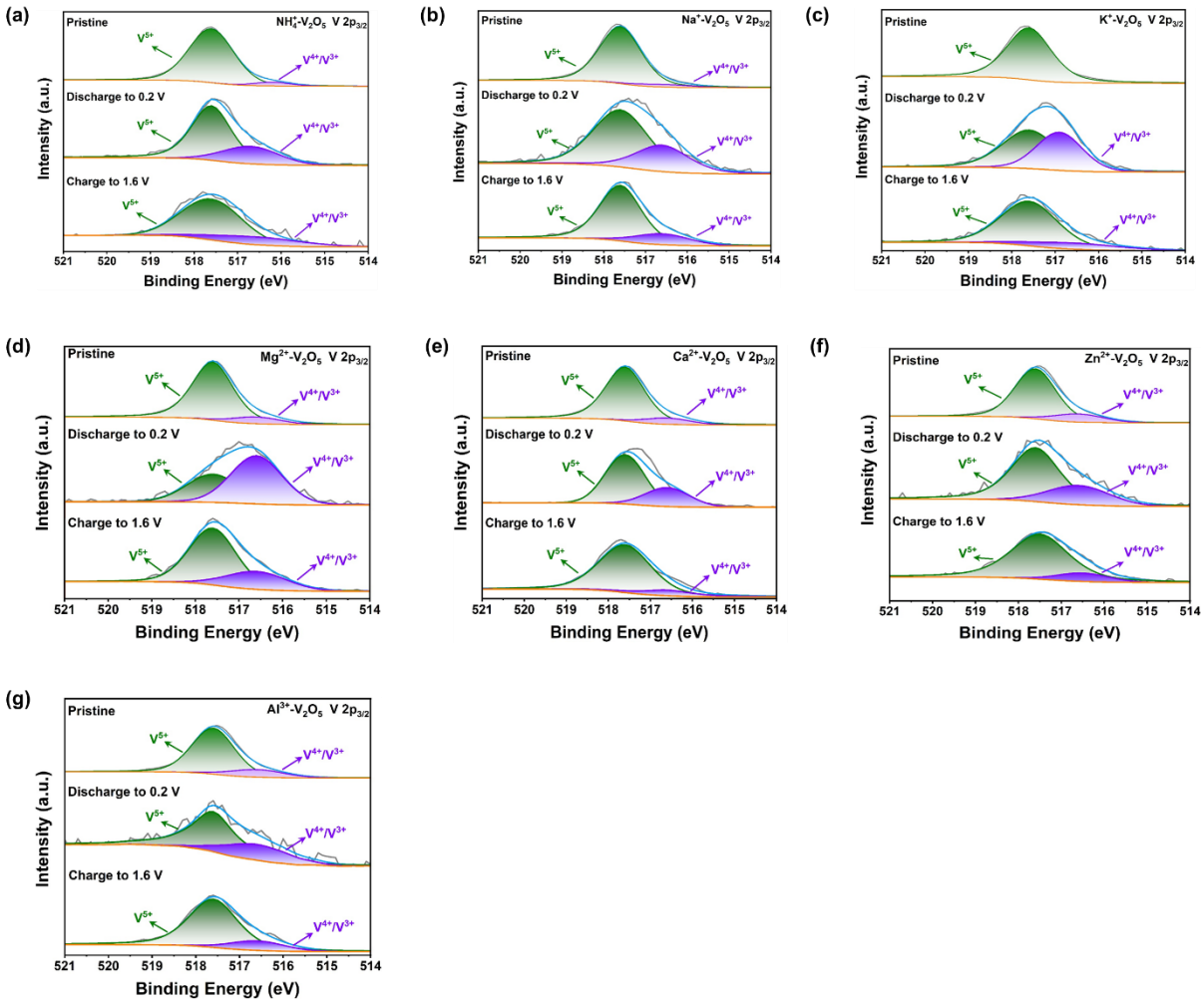

Figure S13. Valence state evolution of V in $M_xV_2O_5{\cdot}nH_2O$ during one cycle. The V $2p_{3/2}$ region (V^{5+}: 517.6 eV; V^{4+}/V^{3+}: 516.6 eV) of the X-ray photoelectron spectroscopic spectra with pristine, discharge to 0.2 V and charge to 1.6 V states of **(a)** NH_4^+, **(b)** Na^+, **(c)** K^+, **(d)** Mg^{2+}, **(e)** Ca^{2+}, **(f)** Zn^{2+}, **(g)** Al^{3+}-based $M_xV_2O_5{\cdot}nH_2O$. For the pristine $(NH_4)_{0.77}V_2O_5{\cdot}0.8H_2O$ cathode, the V $2p_{3/2}$ peaks at 517.6 and 516.6 eV can be attributed to V^{5+} and V^{4+}/V^{3+}, respectively. When discharged to 0.2 V, the proportion of V^{5+} signal is significantly reduced, while the V^{4+} signal become pronounced. When further charged to 1.6 V, the proportion of V^{5+} signal is increased again accompanied by the extraction of Zn^{2+}. This result indicates that V^{5+} are converted to V^{4+}/V^{3+} at the full discharged state. Then the signals of V^{5+} almost recover to the initial intensity at the charged state of 1.6 V, indicating a reversible $V^{5+}\leftrightarrow V^{4+}/V^{3+}$ transformation during Zn^{2+} insertion and extraction.

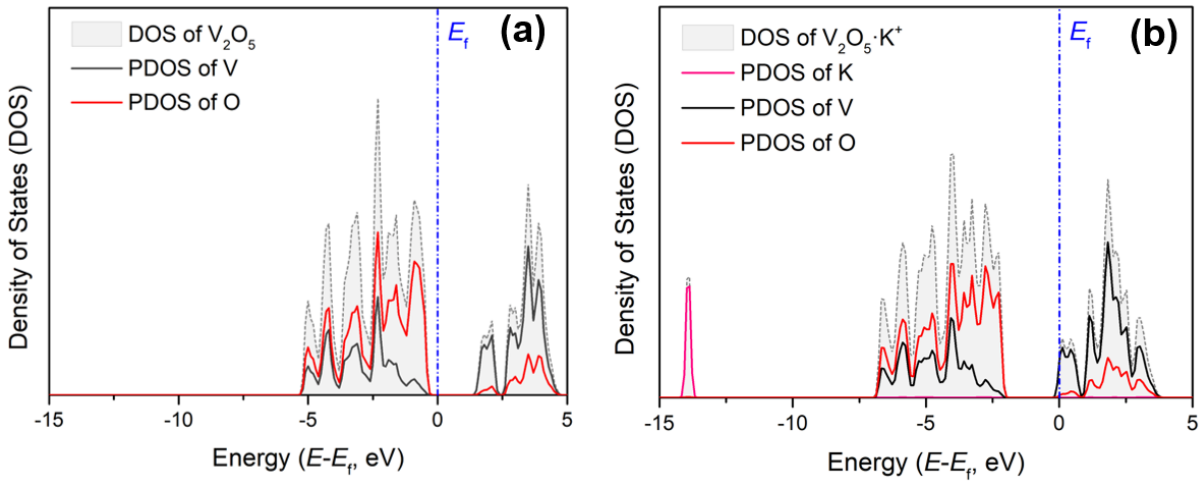

Figure S14. Density of states of (a) V_2O_5 monolayer; (b) K^+ nanoconfinement sample ($K_xV_2O_5$). The V_2O_5 monolayer exhibits the feature of a semiconductor with the valence band maximum (VBM) located below Fermi level and conduction band minimum (CBM) located above Fermi level. A theoretical bandgap of 1.4 eV indicates a poor electronic conductivity. After K^+ nanoconfinement as illustrated in Figure R6b, the bonding features of V_2O_5 substrate generally remains unchanged, showing similar PDOS curves of V and O elements. The K^+ cation mainly yields an isolated peak at around -14 eV relating with the formation of K-O bond.

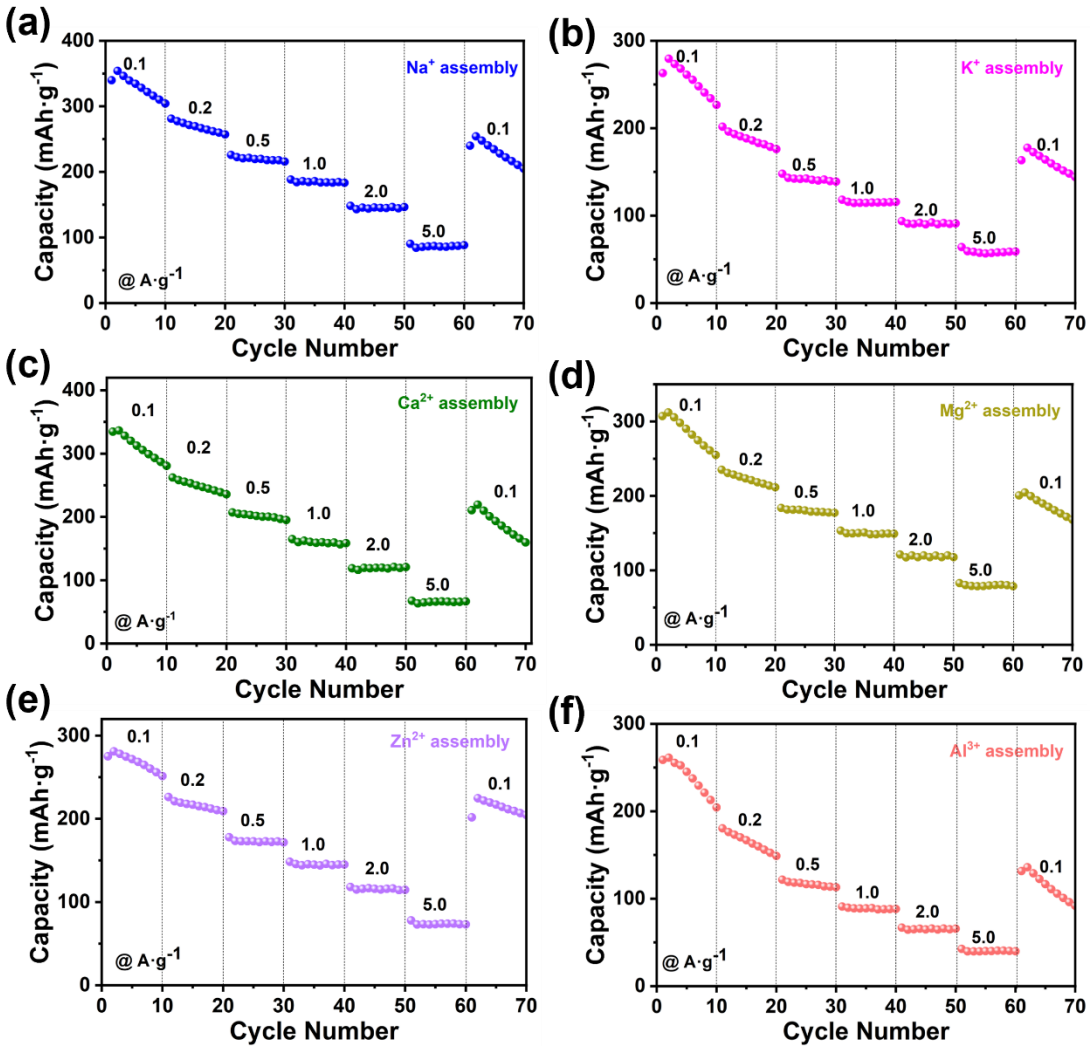

Figure S15. Rate-capability of Na^{+}, K^{+}, Mg^{2+}, Ca^{2+}, Zn^{2+}, Al^{3+} nanoconfinement samples in ultrathin V_2O_5 interlayer.

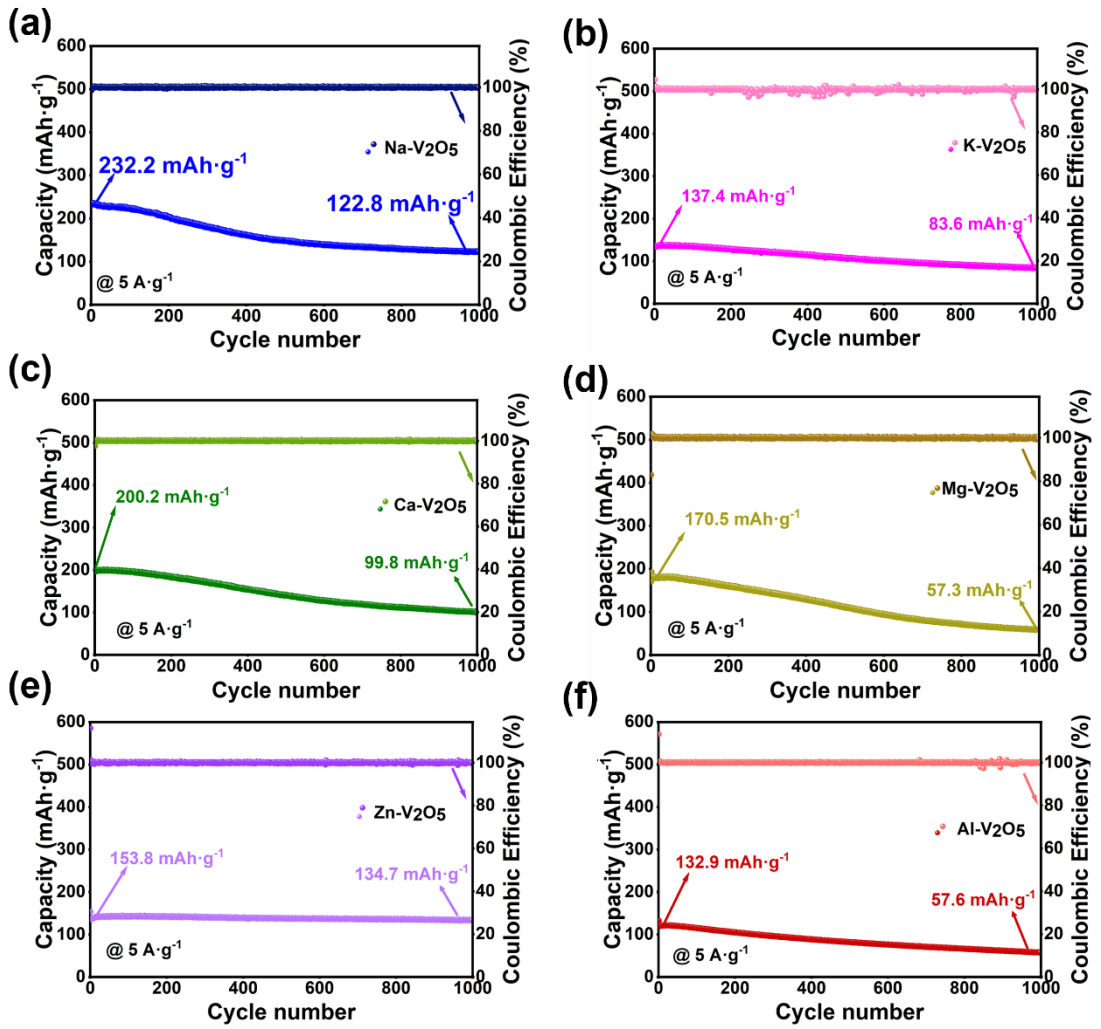

Figure S16. Long-term cycle performance of Na^{+}, K^{+}, Mg^{2+}, Ca^{2+}, Zn^{2+}, Al^{3+} nanoconfinement samples in ultrathin V_2O_5 interlayer at a current density of 5.0 A g^{-1}.

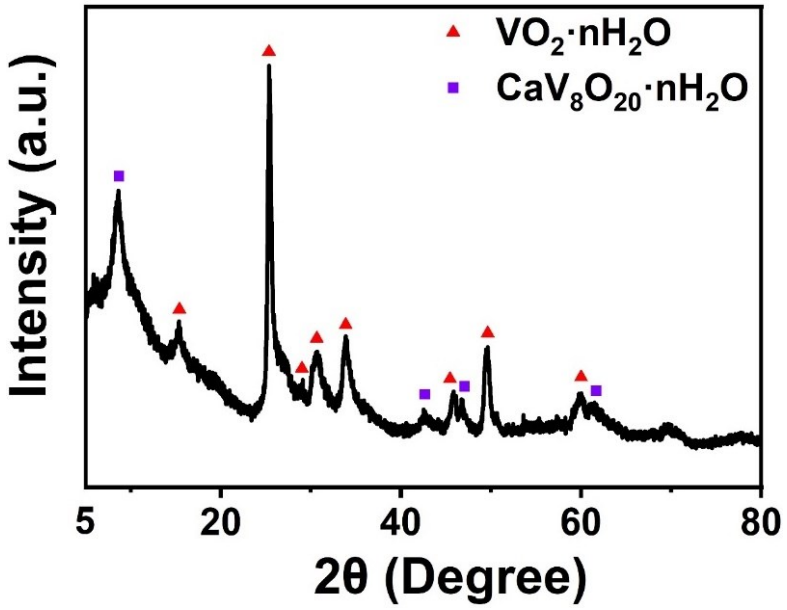

Figure S17. Powder XRD pattern of the hydrothermal product using the similar nanoconfinement cations.

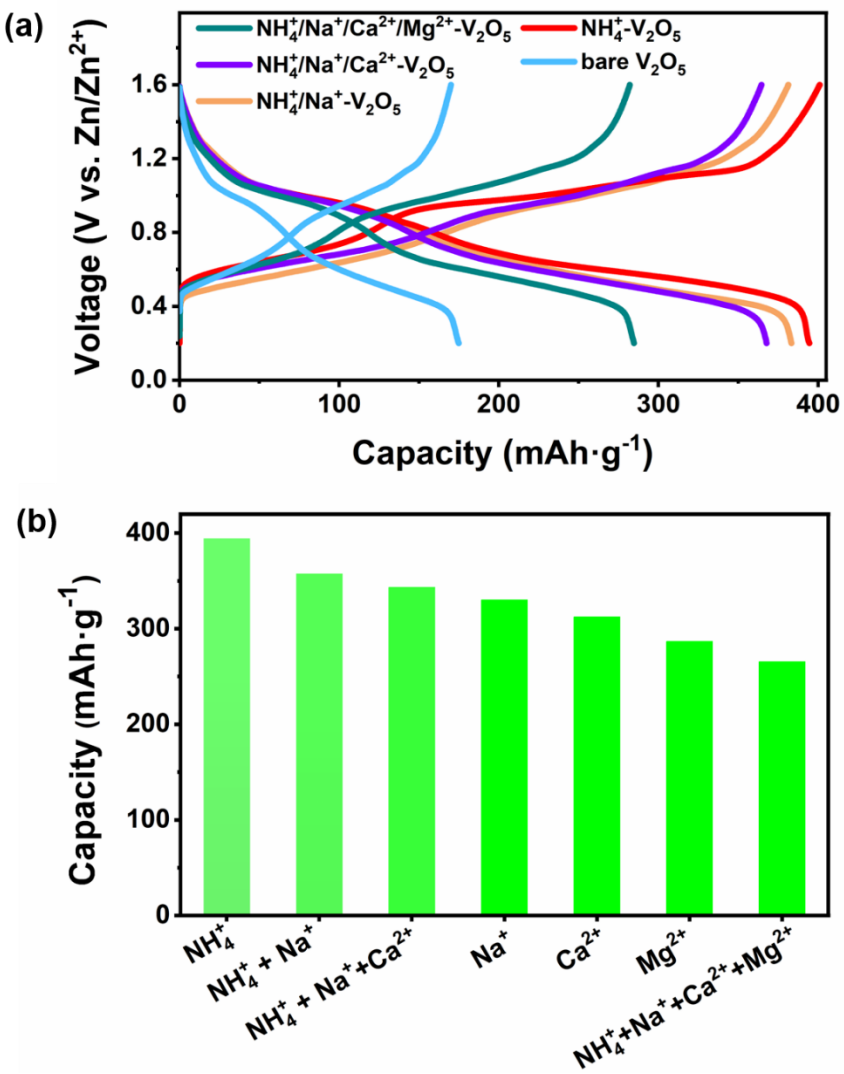

Figure S18. Comparison of the first-cycled discharged capacity of our nanoconfinement series at 0.05 A g^{-1}.

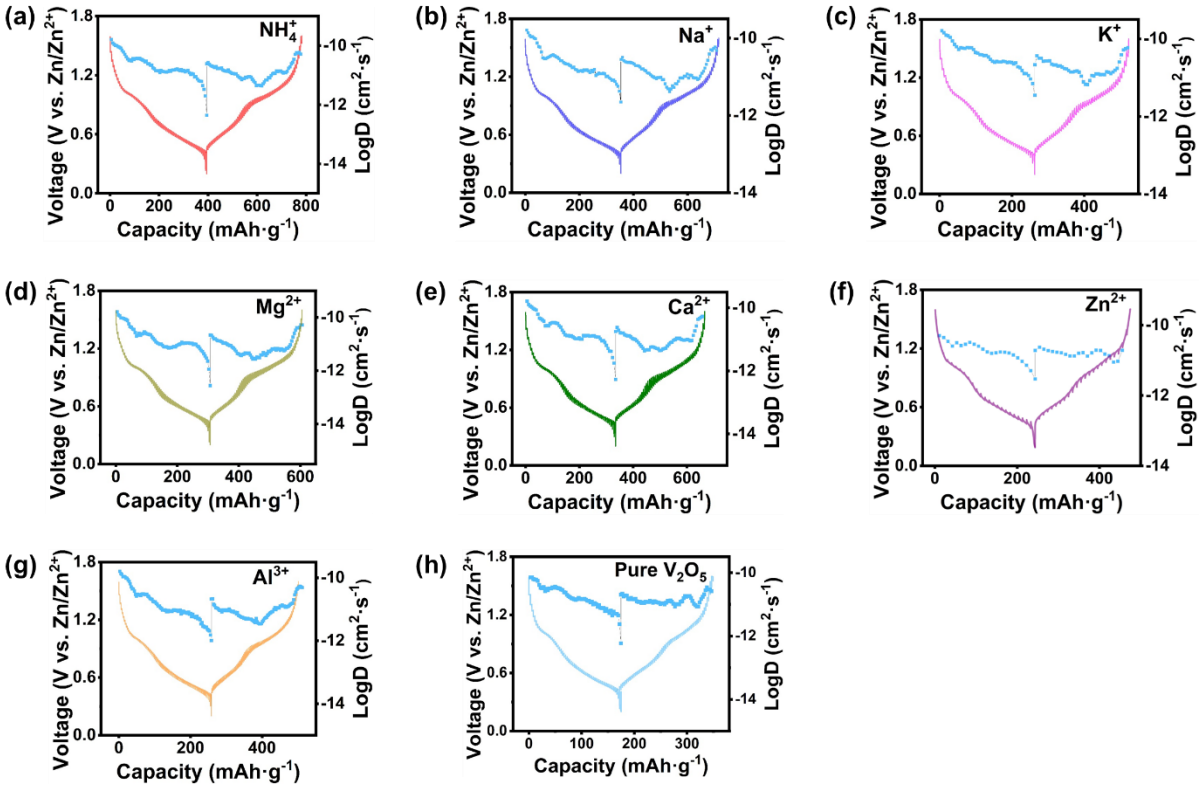

Figure S19. GITT analysis of $M_xV_2O_5{\cdot}nH_2O$ (M: NH_4^+, Na^+, K^+, Mg^{2+}, Ca^{2+}, Zn^{2+}, Al^{3+}) samples by the supramolecular self-assembly. The discharge/charge curves in GITT measurement and the corresponding diffusivity coefficient (D) of Zn^{2+} in the discharge and charge processes of **(a)** NH_4^+, **(b)** Na^+, **(c)** K^+, **(d)** Mg^{2+}, **(e)** Ca^{2+}, **(f)** Zn^{2+}, **(g)** Al^{3+}-based $M_xV_2O_5{\cdot}nH_2O$. **(h)** freeze-dried pure V_2O_5.

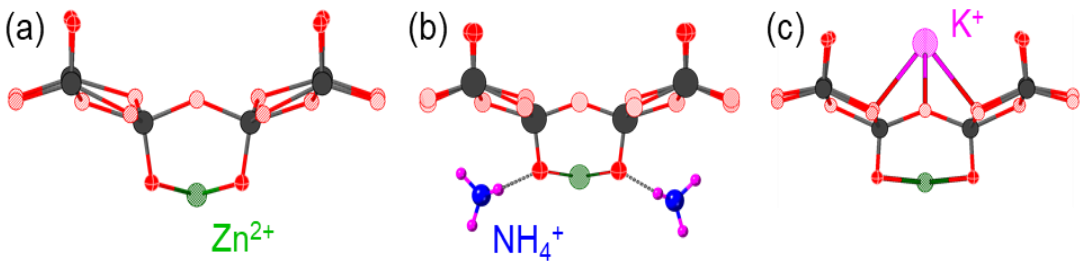

Figure S20. Atomic schemes showing the initial state (minimum energy) of the studied diffusion process: (a) Zn^{2+}-V_2O_5; (b) Zn^{2+}-($V_2O_5{\cdot}NH^{4+}$); (c) Zn^{2+}-($V_2O_5{\cdot}K^+$).

Table S1. Inductive Coupled Plasma Emission Spectrometry (ICP) results of the unitary $M_xV_2O_5{\cdot}nH_2O$ series

Guest cations (M)	M (wt %)	V (wt %)	M (atom %)	V (atom %)	Formula
Na^+	3.08	40.62	3.01	17.91	$Na_{0.34}V_2O_5{\cdot}0.46H_2O$
K^+	5.64	48.71	3.64	24.18	$K_{0.30}V_2O_5{\cdot}0.16H_2O$
Mg^{2+}	1.64	42.71	1.53	19.12	$Mg_{0.16}V_2O_5{\cdot}0.82H_2O$
Ca^{2+}	2.41	44.34	1.41	20.43	$Ca_{0.14}V_2O_5{\cdot}0.72H_2O$
Zn^{2+}	8.21	43.37	3.15	21.25	$Zn_{0.29}V_2O_5{\cdot}0.83H_2O$
Al^{3+}	1.92	37.61	1.55	16.08	$Al_{0.19}V_2O_5{\cdot}1.19H_2O$

Table S2. The chemical component information of the self-assembled products by multiple cations nanoconfinement.

Sample	molar ratio	chemical formula
two cations nanoconfinement	Na: V = 0.15：2.00	$(NH_4)_{0.93}Na_{0.15}V_2O_5{\cdot}0.5H_2O$
three cations nanoconfinement	Na: Ca: V= 0.06: 0.14: 2.00	$(NH_4)_{0.48}Na_{0.06}Ca_{0.14}V_2O_5{\cdot}0.4H_2O$
four cations nanoconfinement	Na: Mg: Ca: V= 0.07: 0.07: 0.18: 2.00	$(NH_4)_{0.52}Na_{0.07}Mg_{0.07}Ca_{0.18}V_2O_5{\cdot}1.3H_2O$